International Journal of Engineering Science 187 (2023) 103842

Contents lists available at ScienceDirect

International Journal of Engineering Science

journal homepage: www.elsevier.com/locate/ijengsci

A continuum large-deformation theory for the coupled modeling of polymer–solvent system with application to PV recycling

Z. Liu [a,b,*], M. Marino [c], J. Reinoso [b], M. Paggi [a]

[a] IMT School for Advanced Studies Lucca, Piazza San Francesco 19, 55100, Lucca, Italy
[b] Departamento de Mecánica de Medios Continuos y Teoría de Estructuras, School of Engineering, Universidad de Sevilla, Camino de los Descubrimientos s/n, 41092, Seville, Spain
[c] Department of Civil Engineering and Computer Science, University of Rome Tor Vergata, Via del Politechnico 1, 00133 Rome, Italy

ARTICLE INFO

Keywords:
Large-deformation
Polymer–solvent system
PV recycling
Finite element method

ABSTRACT

Nowadays recycling of photovoltaics (PV) using the solvent method is becoming a very hot topic as massive products deployed in the last century have approached the end of their service lifetime. The key problem in the recycling of end-of-life PV modules is the nondestructive recovery of precious silicon wafers for the manufacturing of new products. However, the attempt to comprehensively understand the polymer–solvent system in the PV recycling process is completely lacking. In this work, a thermodynamically consistent large-deformation theory is proposed to model the coupled behavior of this system. The development of continuum theory accounts for the solvent permeation, swelling and elastic deformation, as well as shrinking effects due to the initial crosslinking of ethylene-co-vinyl acetate (EVA). The crosslinking of EVA influences the stiffness of the polymer network, and interacts with the diffusive kinetics of solvents. Also, given the effects of mechanical constraint, the two-way coupling between the EVA deformation and solvent diffusion is established on the basis of thermodynamic arguments. The proposed modeling method is firstly applied to simulate the swelling experiments of cylindrical EVA samples in solvents Toluene, Tetrahydrofuran, and Octane, and good agreement has been achieved between the numerical prediction and available testing data. Then the second example demonstrates the capability of this modeling framework to describe the influences of initial crosslinking and mechanical constraints on the time history evolution of swelling and elastic deformation. Finally, the complete PV laminate in the 3D setting is modeled for the investigation of solvent penetration induced deformation in the silicon cell layer during the PV recycling process, and comparison has been made to showcase the spatial distribution of maximum principal stress of the silicon cell layers in solvents with different solubility parameters and molar volumes. With this computational tool at hand, it is possible to provide guidance to the design of suitable experimental procedures for the structure-intact recovery of silicon wafers in PV recycling with the solvent method.

1. Introduction

In the past decades, the development of environmentally friendly energy production techniques has resulted into the fast-growing increase of photovoltaic (PV) modules all over the world (Heath et al., 2020; Köntges et al., 2014, 2017; Tao & Yu, 2015; Weckend, Wade, & Heath, 2016). According to Xu, Lai, Wang, and Wang (2021), it is estimated that the global installed

* Corresponding author at: IMT School for Advanced Studies Lucca, Piazza San Francesco 19, 55100, Lucca, Italy.
E-mail address: zeng.liu@imtlucca.it (Z. Liu).

https://doi.org/10.1016/j.ijengsci.2023.103842
Received 9 November 2022; Received in revised form 9 January 2023; Accepted 27 February 2023
Available online 7 March 2023

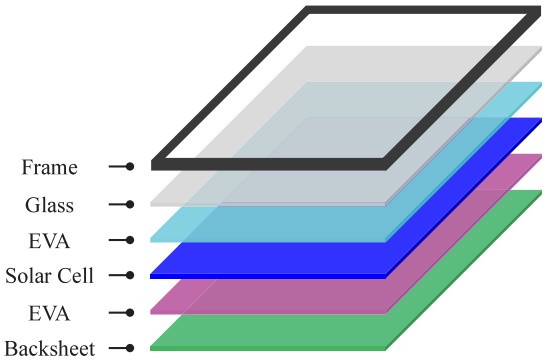

Fig. 1. The general structure of a typical PV module (Liu et al., 2022a).

capacity of PV has dramatically increased from 40 GW to 715 GW in the recent decade. In view of the limited service lifetime (around 25 years) of PV modules (Gagliardi, Lenarda, & Paggi, 2017; Paggi, Berardone, Infuso, & Corrado, 2014; Paggi, Corrado, & Berardone, 2016; Paggi, Corrado, & Rodriguez, 2013), a significant amount of these end-of-life products, which are defined as waste of electronic equipment (Corcelli, Ripa, & Ulgiati, 2017), will continuously pose challenges to the sustainable energy production and environmental protection (Deng, Chang, Ouyang, & Chong, 2019; He, Gutierrez, Young, & Schoenung, 2019; Liu, Reinoso, & Paggi, 2022a; Nain & Kumar, 2020; Tammaro, Salluzzo, Rimauro, Schiavo, & Manzo, 2016). Hence, there is an urgent need to develop reliable techniques to dispose end-of-life PV modules (Cui et al., 2022; Deng, Zhuo, & Shen, 2022; Farrell et al., 2020; Liu, Zhang, & Wang, 2020; Sah, Kumar, et al., 2022; Wang, Tian, Chen, Ren, & Geng, 2022).

The improper disposal of PV panels by landfilling is intolerable nowadays as the hazardous metal components such as lead and cadmium, among others, would cause pollution to the environment (Tammaro et al., 2016). Besides, it is of great importance to recover the precious silicon wafers and other metals for the manufacturing of new products to reduce the cost, supporting the sustainable development of energy production (Bustamante & Gaustad, 2014; Dias et al., 2021; Nevala et al., 2019; Padoan, Altimari, & Pagnanelli, 2019). Normally, the PV module is a laminate structure composing of different plies including tempered glass, silicon solar cells, and backsheet, which are bonded to each other by ethylene-co-vinyl acetate (EVA) layers (Liu, Reinoso, & Paggi, 2022b), as shown in Fig. 1. Therefore, many approaches have been developed in the related literature in order to separate the different layers by the removal of EVA and then reclaim valuable materials in the end-of-life PV modules (Azeumo et al., 2019; Liu et al., 2022a; Lovato, Donato, Lopes, Tanabe, & Bertuol, 2021; Pang et al., 2021). The use of nitric acid to remove EVA layers was proposed in Bruton (1994), but the resulting NO_x emissions are harmful to the environments. Thermal decomposition is another alternative method to remove EVA layers but leads to the release of harmful gas because of the existence of fluorinated compounds (Fiandra, Sannino, Andreozzi, Corcelli and Graditi, 2019; Shin, Park, & Park, 2017; Tammaro, Rimauro, Fiandra, & Salluzzo, 2015). Also, some thermal or mechanical pretreatments are designed to dissemble the backsheet before the further recycling process (Aryan, Font-Brucart, & Maga, 2018; Fiandra, Sannino, Andreozzi and Graditi, 2019; Zhang & Xu, 2016). In addition, recycling of PV modules using the organic solvent method has received a great deal of attention in the recent years (Doi et al., 2001; Kang, Yoo, Lee, Boo, & Ryu, 2012; Kim & Lee, 2012; Li et al., 2022; Prasad, Sanjana, Kiran, Kumar, & Ratheesh, 2022). In spite of these efforts, it is very challenging to reclaim unbroken silicon wafers, which is a key problem in the PV recyling as the thickness of silicon cell layers was reduced to approximately 0.1 mm after 2006 (Huang, Shin, Wang, Sun, & Tao, 2017).

The major factor responsible for the degradation of PV modules is the aging of EVA layers, while the service lifetime of silicon wafers is much longer than that of PV modules (Doi et al., 2001). In this regard, much cost can be saved with the reclaim of structurally intact silicon wafers for the manufacturing of new PV products, since the silicon ingot manufacturing process can be omitted. High environment pollution and energy consumption can be avoided with such an ideal reusing strategy that also reduces around 40% cost of PV production (Liu et al., 2019). Unfortunately, very scarce research activities have been devoted to the nondestructive reclaim of intact silicon wafers in PV recycling, such as thermal decomposition at specific heating rates (Park, Kim, Cho, Lee, & Park, 2016) and breakage of glass layer before thermal treatment (Lee et al., 2018). Although it is possible to recover the intact silicon wafers using the these methods, the thermal decomposition is actually difficult to control and the cracking of glass during the treatment tends to break the silicon wafers. In addition to this, results in Doi et al. (2001) have indicated that the swelling of EVA during the recycling process using the solvent method can lead to the cracking of silicon cell layer. Therefore, there is an urgent need to develop a suitable computational framework to help control the recycling process for the recovery of structurally intact silicon wafers.

EVA is a kind of polymeric material consisting of 3D network of polymer molecules that are bonded to each other, and thus capable of recoverable large-deformation (Baek & Pence, 2009; Drozdov, 2018; Fennell, Leszczynski, Kamphus, & Huyghe, 2020; Mezzasalma, Abrami, Grassi, & Grassi, 2022). During the recycling process using the solvent method, the solvent can penetrate into the EVA network when coming into contact, and the molecules can be absorbed by the skeletal polymeric network of EVA, forming a swollen aggregate. The solvent molecules can interact with each other as well as with the polymer structure, and also migrate in and out of the swollen aggregate. The theory of mass transport in the continuum solids dates back to Tanaka and Fillmore (1979), and

have been further developed for the description of coupled deformation and diffusion with application to the response of hydrogels, including swelling and deswelling induced by mechanical deformation and forced fluid permeation (Bayat, Wang, & Baghani, 2020; Duda, Souza, & Fried, 2010; Sauerwein & Steeb, 2020). The purpose of this work is to develop a thermodynamically consistent large-deformation theory on the continuum level for the description of EVA polymer–solvent system in the PV recycling, so as to provide guidance to the design of experimental procedures for the nondestructive recovery of ultrathin and brittle silicon wafers. Similarly to the theories developed by Duda et al. (2010), the polymer–solvent system is treated as homogenized continuum in which the solvent flux is allowed. In the development of constitutive theory, the Flory–Huggins theory for the free energy change due to the mixing of solvents with different solubility parameters and EVA polymer network is adopted, and the statistical–mechanical model is accounted for to describe the entropic change of EVA polymer chains due to the mechanical stretching.

This work proposes a computational framework at finite strains for the modeling of EVA polymer–solvent system in PV recycling using the solvent method, which takes into account the coupled solvent diffusion, swelling and shrinking of EVA polymers, as well as effects of mechanical constraints and initial crosslinking of EVA during PV lamination. In Sections 2 and 3, the basic continuum kinematics in the large-deformation framework and balance laws for force and mass balance are given according to the standard modern continuum mechanics. Section 4 presents the derivation of thermodynamics and constitutive theory, and the specific free energy definition is given in Section 5. The numerical implementation of this theory is derived in detail using the finite element method in Section 6, and then applied to the PV recycling through some examples in Section 7. Finally some concluding remarks are presented in Section 8.

2. Continuum kinematics

According to the standard concepts of continuum mechanics framework (Gurtin, Fried, & Anand, 2010; Wriggers, 2008), the EVA body in PV modules can be described as a macroscopically homogeneous continuum solid within the Euclidean space $\mathbb{E}^3$. It is assumed that kinematic fields in the continuum theory are applied at large length scales compared to that associated with the polymer molecule network and pore-structure of EVA (Dortdivanlioglu & Linder, 2019; Hajikhani, Wriggers, & Marino, 2021). We identify the macroscopically homogeneous EVA with the space it occupies in the reference configuration $\mathcal{B}_0$, and describe the current configuration $\mathcal{B}$ by a smooth one-to-one transformation mapping $\boldsymbol{\varphi} : \mathcal{B}_0 \to \mathbb{E}^3$. The position vector of an arbitrary material point in the reference configuration $\mathcal{B}_0$ is denoted by $\mathbf{X}$, and the corresponding vector in the current configuration $\mathcal{B}$ is represented by $\mathbf{x} = \boldsymbol{\varphi}(\mathbf{X}, t)$.

The displacement field in the reference configuration is defined as $\mathbf{u}(\mathbf{X}, t) = \mathbf{x} - \mathbf{X} = \boldsymbol{\varphi}(\mathbf{X}, t) - \mathbf{X}$, and the transformation mapping is described by the deformation gradient $\mathbf{F}$, which reads

$$\mathbf{F} = \frac{\partial \boldsymbol{\varphi}(\mathbf{X}, t)}{\partial \mathbf{X}} = \nabla_{\mathbf{X}} \boldsymbol{\varphi}(\mathbf{X}, t) \tag{1}$$

where $\nabla_{\mathbf{X}}$ denotes the material gradient. The determinant of the deformation gradient is defined as $J = \det \mathbf{F} \neq 0$, representing the volume change from the reference configuration to the current configuration. The velocity $\mathbf{v}$ and its gradient with respect to the position vector $\mathbf{x}$ in the current configuration $\mathbf{L}$ are given by

$$\mathbf{v} = \dot{\boldsymbol{\varphi}}(\mathbf{X}, t) \quad \text{and} \quad \mathbf{L} = \nabla_{\mathbf{x}} \mathbf{v} = \dot{\mathbf{F}} \cdot \mathbf{F}^{-1} \tag{2}$$

where $\nabla_{\mathbf{x}}$ denotes the spatial gradient.

To describe the coupled mechanical behavior of polymer and solvent, the multiplicative decomposition of deformation gradient is given by

$$\mathbf{F} = \mathbf{F}^e \cdot \mathbf{F}^s \tag{3}$$

where $\mathbf{F}^e$ and $\mathbf{F}^s$ represent the elastic and swelling parts of deformation gradient $\mathbf{F}$, respectively. The swelling distortion $\mathbf{F}^s$ is defined as

$$\mathbf{F}^s = \lambda^s \mathbf{1}, \quad \text{with} \quad \lambda^s \geq 0 \tag{4}$$

where λ^s is the swelling stretch, which accounts for the swelling of the polymeric body due to absorbed solvents that are pinned to the network structure in the intermediate local space at the material point $\mathbf{X}$. For convenience, the determinant J can be written as

$$J = J^e J^s, \quad \text{with} \quad J^e = \det \mathbf{F}^e \quad \text{and} \quad J^s = \det \mathbf{F}^s = (\lambda^s)^3 \tag{5}$$

Remarkably, $(J^s - 1)$ represents the volume change per unit reference volume of EVA resulting from the swelling behavior due to the change in the solvent content. Analogous to the theory developed for hydrogels, the swelling constraint is defined as

$$J^s = 1 + \upsilon C_{\mathrm{R}} \quad \text{and} \quad \phi = (1 + \upsilon C_{\mathrm{R}})^{-1} \tag{6}$$

where υ denotes the volume of a mole of solvent molecules, C_{R} represents the number of moles of absorbed solvent molecules by the polymeric body per unit reference volume, and ϕ is the polymer volume fraction.

Following the standard decomposition of deformation gradient, we have

$$\mathbf{F} = \mathbf{R} \cdot \mathbf{U} = \mathbf{V} \cdot \mathbf{R} \quad \text{and} \quad \mathbf{F}^e = \mathbf{R}^e \cdot \mathbf{U}^e = \mathbf{V}^e \cdot \mathbf{R}^e \tag{7}$$

where $\mathbf{R}$ and $\mathbf{R}^e$ are rotation tensors, $\mathbf{U}$ and $\mathbf{U}^e$ are right stretching tensors, and $\mathbf{V}$ and $\mathbf{V}^e$ are left stretching tensors. Subsequently, the total right and left Cauchy–Green tensors $\mathbf{C}$ and $\mathbf{B}$, and the elastic corresponding tensors $\mathbf{C}^e$ and $\mathbf{B}^e$ are defined as

$$\mathbf{C} = \mathbf{U}^2 = \mathbf{F}^{\mathrm{T}} \cdot \mathbf{F} \quad \text{and} \quad \mathbf{B} = \mathbf{V}^2 = \mathbf{F} \cdot \mathbf{F}^{\mathrm{T}} \tag{8a}$$

$$\mathbf{C}^e = \mathbf{U}^{e2} = \mathbf{F}^{e\mathrm{T}} \cdot \mathbf{F}^e \quad \text{and} \quad \mathbf{B}^e = \mathbf{V}^{e2} = \mathbf{F}^e \cdot \mathbf{F}^{e\mathrm{T}} \tag{8b}$$

Next, by substituting Eq. (3) into Eq. $(2)_2$, the velocity tensor $\mathbf{L}$ can be expressed as

$$\mathbf{L} = \mathbf{L}^e + \mathbf{F}^e \cdot \mathbf{L}^s \cdot \mathbf{F}^{e-1} \tag{9}$$

where the elastic and swelling velocity tensors $\mathbf{L}^e$ and $\mathbf{L}^s$ are given by

$$\mathbf{L}^e = \dot{\mathbf{F}}^e \cdot \mathbf{F}^{e-1} \quad \text{and} \quad \mathbf{L}^s = \dot{\mathbf{F}}^s \cdot \mathbf{F}^{s-1} \tag{10}$$

3. Balance laws

3.1. Balance of linear and angular momentum

In the current configuration, the local form of force balance in the absence of dynamic effects can be expressed as

$$\nabla_{\mathbf{x}} \cdot \boldsymbol{\sigma} + \mathbf{b} = \mathbf{0} \tag{11}$$

where $\mathbf{b}$ is the body force per unit deformed body, and $\boldsymbol{\sigma}$ is the Cauchy stress tensor deriving from the balance of angular momentum. As is standard (Zäh & Miehe, 2015), the first Piola–Kirchhoff stress tensor $\mathbf{P}$ and Kirchhoff stress tensor $\boldsymbol{\tau}$ can be related to the symmetric Cauchy stress tensor $\boldsymbol{\sigma}$ by

$$\mathbf{P} = J\boldsymbol{\sigma} \cdot \mathbf{F}^{-\mathrm{T}} \tag{12a}$$

$$\boldsymbol{\tau} = J\boldsymbol{\sigma} \tag{12b}$$

and thus

$$\boldsymbol{\sigma} = J^{-1}\mathbf{P} \cdot \mathbf{F}^{\mathrm{T}} \tag{13}$$

Let $\partial\mathcal{B}_{\mathbf{u}}$ and $\partial\mathcal{B}_{\mathbf{t}}$ be the complementary surfaces of the polymeric body $\mathcal{B}$ with $\partial\mathcal{B} = \partial\mathcal{B}_{\mathbf{u}} \cup \partial\mathcal{B}_{\mathbf{t}}$ and $\partial\mathcal{B}_{\mathbf{u}} \cap \partial\mathcal{B}_{\mathbf{t}} = \varnothing$. The boundary conditions imposed on the body in the current configuration can be given by

$$\mathbf{u} = \bar{\mathbf{u}} \quad \text{on} \quad \partial\mathcal{B}_{\mathbf{u}} \tag{14a}$$

$$\boldsymbol{\sigma} \cdot \mathbf{n} = \bar{\mathbf{t}} \quad \text{on} \quad \partial\mathcal{B}_{\mathbf{t}} \tag{14b}$$

where $\mathbf{n}$ is the outward unit normal on the external boundary $\partial\mathcal{B}$ of the body $\mathcal{B}$.

3.2. Mass balance of the solvent content

Let $\mathbf{j}$ denotes the fluid flux per unit deformed area per unit time, and thus $-\int_{\partial\mathcal{B}} \mathbf{j} \cdot \mathbf{n}\, \mathrm{d}\partial\Omega$ represents the total moles of solvent molecules entering the EVA body $\mathcal{B}$ across $\partial\mathcal{B}$ per unit time. In the current configuration, the mass balance equation reads

$$\dot{C}_{\mathrm{R}} = -J\nabla_{\mathbf{x}} \cdot \mathbf{j} \tag{15}$$

By the substitution of Eq. $(6)_2$, Eq. (15) can be rewritten as

$$\frac{\dot{\phi}}{J\upsilon\phi^2} - \nabla_{\mathbf{x}} \cdot \mathbf{j} = 0 \tag{16}$$

in which the fluid flux $\mathbf{j}$ is defined as (Duda et al., 2010)

$$\mathbf{j} = -m(\phi) \cdot \nabla_{\mathbf{x}}\mu \quad \text{with} \quad m(\phi) = \frac{D}{RT\upsilon}\left[(1-\gamma)\phi + \gamma\right] \tag{17}$$

where m is the mobility coefficient that depends on the polymer volume fraction ϕ and diffusion coefficient D, R is the universal gas constant, T represents the absolute temperature, and γ is the correlation coefficient that determines the change of polymer network due to the increase of solvent content.

Let $\partial\mathcal{B}_{\mu}$ and $\partial\mathcal{B}_{\mathbf{j}}$ be the complementary surfaces of the polymeric body $\mathcal{B}$ with $\partial\mathcal{B} = \partial\mathcal{B}_{\mu} \cup \partial\mathcal{B}_{\mathbf{j}}$ and $\partial\mathcal{B}_{\mu} \cap \partial\mathcal{B}_{\mathbf{j}} = \varnothing$. The boundary conditions imposed on the EVA body in the current configuration are given by

$$\mu = \bar{\mu} \quad \text{on} \quad \partial\mathcal{B}_{\mu} \tag{18a}$$

$$-\mathbf{j} \cdot \mathbf{n} = \bar{j} \quad \text{on} \quad \partial\mathcal{B}_{\mathbf{j}} \tag{18b}$$

where μ is the chemical potential that will be derived in the following.

4. Thermodynamics and constitutive laws

4.1. Second law of thermodynamics

Following the discussion of thermodynamics and ignoring inertial effects and kinetic energy (Gurtin et al., 2010), the balance law for energy under the isothermal condition using Lagrangian description is given by

$$\int_{\mathcal{B}_0} \dot{\psi}_{\mathrm{R}}\ \mathrm{d}\Omega_{\mathrm{R}} \leq \int_{\partial\mathcal{B}_0} \left(\mathbf{P}\cdot\mathbf{N}_{\mathrm{R}}\right)\cdot\dot{\boldsymbol{\varphi}}\ \mathrm{d}\partial\Omega_{\mathrm{R}} + \int_{\mathcal{B}_0} \mathbf{B}_{\mathrm{R}}\cdot\dot{\boldsymbol{\varphi}}\ \mathrm{d}\Omega_{\mathrm{R}} - \int_{\partial\mathcal{B}_0} \mu\mathbf{J}_{\mathrm{R}}\cdot\mathbf{N}_{\mathrm{R}}\ \mathrm{d}\partial\Omega_{\mathrm{R}} \tag{19}$$

where the subscript R means the description of fields in the reference configuration, $\mathbf{J}_{\mathrm{R}}$ is the solvent fluid flux in the reference configuration that is pulled back from the current configuration (i.e., $\mathbf{J}_{\mathrm{R}} = J\mathbf{F}^{-1}\cdot\mathbf{j}$), $\mathbf{N}_{\mathrm{R}}$ stands for the unit normal in the reference configuration, $\mathbf{B}_{\mathrm{R}}$ represents the body force in the reference configuration, and ψ_{R} denotes the Helmholtz free energy density per unit reference volume. By using the divergence theorem, Eq. (19) can be rewritten as

$$\int_{\mathcal{B}_0} \left[\dot{\psi}_{\mathrm{R}} - \left(\nabla_{\mathbf{X}}\cdot\mathbf{P} + \mathbf{B}_{\mathrm{R}}\right)\cdot\dot{\boldsymbol{\varphi}} - \mathbf{P}:\dot{\mathbf{F}} + \mu\ \nabla_{\mathbf{X}}\cdot\mathbf{J}_{\mathrm{R}} + \mathbf{J}_{\mathrm{R}}\cdot\nabla_{\mathbf{X}}\mu\right]\ \mathrm{d}\Omega_{\mathrm{R}} \leq 0 \tag{20}$$

Given the material description of Eqs. (11) and (15), and using the fact that Eq. (20) must hold for every part of the EVA body, the local form of energy imbalance in the reference configuration is given by

$$\dot{\psi}_{\mathrm{R}} - \mathbf{P}:\dot{\mathbf{F}} - \mu\dot{C}_{\mathrm{R}} + \mathbf{J}_{\mathrm{R}}\cdot\nabla_{\mathbf{X}}\mu \leq 0 \tag{21}$$

By using Eqs. (3), (9), (10), and (12a), the stress-power term can be written as

$$\begin{aligned}
\mathbf{P}:\dot{\mathbf{F}} &= J\left(\boldsymbol{\sigma}\cdot\mathbf{F}^{-\mathrm{T}}\right):\dot{\mathbf{F}} = J\boldsymbol{\sigma}:\left(\mathbf{L}^{e} + \mathbf{F}^{e}\cdot\mathbf{L}^{s}\cdot\mathbf{F}^{e-1}\right)\\
&= J\boldsymbol{\sigma}:\left(\dot{\mathbf{F}}^{e}\cdot\mathbf{F}^{e-1}\right) + J\boldsymbol{\sigma}:\left(\mathbf{F}^{e}\cdot\mathbf{L}^{s}\cdot\mathbf{F}^{e-1}\right)\\
&= J\boldsymbol{\sigma}:\left(\dot{\mathbf{F}}^{e}\cdot\mathbf{F}^{e-1}\right) + J\left(\mathbf{F}^{e\mathrm{T}}\cdot\boldsymbol{\sigma}\cdot\mathbf{F}^{e-\mathrm{T}}\right):\mathbf{L}^{s}\\
&= \frac{1}{2}J\left(\mathbf{F}^{e-1}\cdot\boldsymbol{\sigma}\cdot\mathbf{F}^{e-\mathrm{T}}\right):\dot{\mathbf{C}}^{e} + J\left(\mathbf{F}^{e\mathrm{T}}\cdot\boldsymbol{\sigma}\cdot\mathbf{F}^{e-\mathrm{T}}\right):\mathbf{L}^{s}
\end{aligned} \tag{22}$$

For convenience, two stress measures are defined as

$$\mathbf{S}^{e} = J\mathbf{F}^{e-1}\cdot\boldsymbol{\sigma}\cdot\mathbf{F}^{e-\mathrm{T}} \quad \text{and} \quad \mathbf{M}^{e} = J\mathbf{F}^{e\mathrm{T}}\cdot\boldsymbol{\sigma}\cdot\mathbf{F}^{e-\mathrm{T}} \tag{23}$$

so that

$$\mathbf{P}:\dot{\mathbf{F}} = \frac{1}{2}\ \mathbf{S}^{e}:\dot{\mathbf{C}}^{e} + \mathbf{M}^{e}:\mathbf{L}^{s} \tag{24}$$

where $\mathbf{S}^{e}$ and $\mathbf{M}^{e}$ are the second Piola stress tensor and Mandel stress tensor, respectively. Given Eqs. (4), (5) and (10), the stress-power Eq. (24) can be written as

$$\begin{aligned}
\mathbf{P}:\dot{\mathbf{F}} &= \frac{1}{2}\ \mathbf{S}^{e}:\dot{\mathbf{C}}^{e} + \mathbf{M}^{e}:\left(\dot{\mathbf{F}}^{s}\cdot\mathbf{F}^{s-1}\right)\\
&= \frac{1}{2}\ \mathbf{S}^{e}:\dot{\mathbf{C}}^{e} + \frac{1}{3}J^{s-1}\dot{J}^{s}\mathbf{M}^{e}:\mathbf{1}\\
&= \frac{1}{2}\ \mathbf{S}^{e}:\dot{\mathbf{C}}^{e} - \bar{p}\dot{J}^{s}
\end{aligned} \tag{25}$$

in which $\bar{p}$ is the mean normal pressure defined as $\bar{p} = -\frac{1}{3}J^{s-1}\mathbf{M}^{e}:\mathbf{1}$. Hence, by substituting Eq. (25) into Eq. (21), the local form of free energy imbalance in the reference configuration is given by

$$\dot{\psi}_{\mathrm{R}} - \frac{1}{2}\ \mathbf{S}^{e}:\dot{\mathbf{C}}^{e} + \bar{p}\dot{J}^{s} - \mu\dot{C}_{\mathrm{R}} + \mathbf{J}_{\mathrm{R}}\cdot\nabla_{\mathbf{X}}\mu \leq 0 \tag{26}$$

Recalling Eq. (6), it results into $\dot{J}^{s} = \upsilon\dot{C}_{\mathrm{R}}$ that yields

$$\dot{\psi}_{\mathrm{R}} - \frac{1}{2}\ \mathbf{S}^{e}:\dot{\mathbf{C}}^{e} - (\mu - \upsilon\bar{p})\dot{C}_{\mathrm{R}} + \mathbf{J}_{\mathrm{R}}\cdot\nabla_{\mathbf{X}}\mu \leq 0 \tag{27}$$

4.2. Constitutive theory

The Helmholtz free energy ψ_{R} is assumed to depend on the deformation $\mathbf{C}^{e}$, solvent concentration C_{R}, and thus its rate is given by

$$\dot{\psi}_{\mathrm{R}}\left(\mathbf{C}^{e}, C_{\mathrm{R}}\right) = \frac{\partial\psi_{\mathrm{R}}}{\partial\mathbf{C}^{e}}:\dot{\mathbf{C}}^{e} + \frac{\partial\psi_{\mathrm{R}}}{\partial C_{\mathrm{R}}}\dot{C}_{\mathrm{R}} \tag{28}$$

Eq. (27) yields,

$$\left(\frac{\partial\psi_{\mathrm{R}}}{\partial\mathbf{C}^{e}} - \frac{1}{2}\ \mathbf{S}^{e}\right):\dot{\mathbf{C}}^{e} - \left[\frac{\partial\psi_{\mathrm{R}}}{\partial C_{\mathrm{R}}} - (\mu - \upsilon\bar{p})\right]\dot{C}_{\mathrm{R}} + \mathbf{J}_{\mathrm{R}}\cdot\nabla_{\mathbf{X}}\mu \leq 0 \tag{29}$$

Given that this inequality should hold for any values of $\mathbf{C}^e$ and C_{R}, the following thermodynamics restrictions can be obtained

$$\mathbf{S}^e = 2\frac{\partial \psi_{\mathrm{R}}\left(\mathbf{C}^e, C_{\mathrm{R}}\right)}{\partial \mathbf{C}^e} \quad \text{and} \quad \mu = \frac{\partial \psi_{\mathrm{R}}\left(\mathbf{C}^e, C_{\mathrm{R}}\right)}{\partial C_{\mathrm{R}}} + \upsilon \bar{p} \tag{30}$$

Next, recalling Eqs. (12a) and (23), the Piola stress tensor and Cauchy stress tensor can be written as

$$\boldsymbol{\sigma} = 2J^{-1}\mathbf{F}^e \cdot \frac{\partial \psi_{\mathrm{R}}\left(\mathbf{C}^e, C_{\mathrm{R}}\right)}{\partial \mathbf{C}^e} \cdot \mathbf{F}^{e\mathrm{T}} \tag{31a}$$

$$\mathbf{P} = 2\mathbf{F}^e \cdot \frac{\partial \psi_{\mathrm{R}}\left(\mathbf{C}^e, C_{\mathrm{R}}\right)}{\partial \mathbf{C}^e} \cdot \mathbf{F}^{s-\mathrm{T}} \tag{31b}$$

Notably, in view of Eq. (17), the solvent-transport inequality is followed

$$\mathbf{J}_{\mathrm{R}} \cdot \nabla_{\mathbf{X}} \mu = -Jm\|\nabla_{\mathbf{x}} \mu\|^2 \leq 0 \tag{32}$$

5. Free energy definition

Following the well-established methods (Hajikhani et al., 2021), the Helmholtz free energy ψ_{R} can be specialized as

$$\psi_{\mathrm{R}}\left(\mathbf{C}^e, C_{\mathrm{R}}\right) = \bar{\mu}_{\mathrm{R}} C_{\mathrm{R}} + \psi_{\mathrm{R,mech}}\left(\mathbf{C}^e, C_{\mathrm{R}}\right) + \psi_{\mathrm{R,mix}}\left(\mathbf{C}^e, C_{\mathrm{R}}\right) \tag{33}$$

where $\bar{\mu}_{\mathrm{R}}$ is the reference chemical potential of the solvent, $\psi_{\mathrm{R,mech}}\left(\mathbf{C}^e, C_{\mathrm{R}}\right)$ denotes the mechanical contribution to the free energy, and $\psi_{\mathrm{R,mix}}\left(\mathbf{C}^e, C_{\mathrm{R}}\right)$ represents the energy contribution due to the mixing of the solvent with the EVA body.

The mixing free energy per unit reference volume of the polymeric body is defined as

$$\psi_{\mathrm{R,mix}}\left(\mathbf{C}^e, C_{\mathrm{R}}\right) = RTC_{\mathrm{R}} \ln\left(\frac{\upsilon C_{\mathrm{R}}}{1+\upsilon C_{\mathrm{R}}}\right) + RT\chi\left(\frac{C_{\mathrm{R}}}{1+\upsilon C_{\mathrm{R}}}\right) \tag{34}$$

where χ is the dimensionless parameter. Recalling the definition of polymer volume fraction in Eq. (6), the mixing free energy in Eq. (34) can be written as

$$\psi_{\mathrm{R,mix}}\left(\mathbf{C}^e, C_{\mathrm{R}}\right) = RT\frac{1-\phi}{\upsilon\phi}\ln(1-\phi) + RT\frac{\chi(1-\phi)}{\upsilon} \tag{35}$$

It should be pointed out that the enthalpy term in Eq. (34) is introduced for the mixing of polymer–solvent system in line with the Flory–Huggins theory. According to Díez, Camacho, Díaz, and Ovejero (2014), the Flory–Huggins parameter χ can be determined as

$$\chi = \chi_S + \chi_H = \chi_S + \frac{\upsilon}{RT}\left(\delta_s - \delta_p\right)^2 \tag{36}$$

where χ_S and χ_H are the entropic and enthalphic contributions of the parameter, respectively, δ_p is the solubility parameter of polymer, and δ_s is the solubility parameter of the specific solvent, which is given by

$$\delta_s = \left(\delta_{s,d}^2 + \delta_{s,p}^2 + \delta_{s,h}^2\right)^{1/2} \tag{37}$$

where $\delta_{s,d}$ is the apolar part, $\delta_{s,p}$ is the polar part, and $\delta_{s,h}$ is the hydrogen bonding part.

By coupling an energetic contribution with a Gaussian statistics based entropic term (Chester & Anand, 2011), the mechanical free energy $\psi_{\mathrm{R,mech}}$ can be expressed as

$$\psi_{\mathrm{R,mech}} = \frac{1}{2}G(\alpha)\left(\phi^{-2/3}\mathbf{C}^e : \mathbf{1} - 2\ln J - 3\right) + \frac{1}{2}K(\alpha)(\ln J^e)^2 \tag{38}$$

where α is the crosslinking degree during the lamination process, and $G(\alpha)$ and $K(\alpha)$ represent the shear modulus and bulk modulus of EVA polymer network, respectively. To account for the crosslinking effects on polymer structure (Espinasse, Cassagnau, Bert, & Michel, 1994; Schulze, Apel, Daßler, & Ehrich, 2015; Wallner, Adothu, Pugstaller, Costa, & Mallick, 2022), the shear modulus is assumed to depend on the gelation, and defined as

$$G(\alpha) = (1-\alpha)G^0 + \alpha G^1 \tag{39}$$

in which G^0 is the shear modulus of polymer network with no crosslinking ($\alpha = 0$), and G^1 is the shear modulus of polymer network with full crosslinking ($\alpha = 1$). As a result of Eq. (39), the bulk modulus can be determined as

$$K(\alpha) = \frac{2G(\alpha)(1+\nu)}{3(1-2\nu)} \tag{40}$$

where ν denotes the Poisson's ratio of the polymer network.

Thus, using Eqs. (35) and (38) in Eq. (33), the free energy function accounting for the combination of mixing, swelling and elastic stretching effects takes the form of

$$\begin{aligned}\psi_{\mathrm{R}}\left(\mathbf{C}^e, C_{\mathrm{R}}\right) =& \bar{\mu}_{\mathrm{R}} C_{\mathrm{R}} + RT\frac{1-\phi}{\upsilon\phi}\ln(1-\phi) + RT\frac{\chi(1-\phi)}{\upsilon} \\ &+ \frac{1}{2}G(\alpha)\left(\phi^{-2/3}\mathbf{C}^e : \mathbf{1} - 2\ln J - 3\right) + \frac{1}{2}K(\alpha)(\ln J^e)^2\end{aligned} \tag{41}$$

Recalling Eq. (31a), the Cauchy stress tensor is given by

$$\boldsymbol{\sigma} = J^{-1}\left[G(\alpha)\phi^{-2/3}\mathbf{B}^e - G(\alpha)\mathbf{1} + K(\alpha)\left(\ln J^e\right)\mathbf{1}\right] \tag{42}$$

Next, by the use of

$$\mathbf{B} = \mathbf{F}\cdot\mathbf{F}^T = \phi^{-2/3}\mathbf{B}^e \tag{43}$$

Eq. (42) reduces to

$$\boldsymbol{\sigma} = J^{-1}\left[G(\alpha)\left(\mathbf{B} - \mathbf{1}\right) + K(\alpha)\left(\ln J^e\right)\mathbf{1}\right] \tag{44}$$

Hence, according to Eq. (31a), the first Piola–Kirchhoff stress tensor is given by

$$\mathbf{P} = G(\alpha)\left(\mathbf{F} - \mathbf{F}^{-\mathrm{T}}\right) + K(\alpha)\left(\ln J^e\right)\mathbf{F}^{-\mathrm{T}} \tag{45}$$

Also, using Eqs. $(30)_2$ and (41) and taking into account $J = J^e/\phi = J^e(1 + \upsilon C_{\mathrm{R}})$, the chemical potential μ is given by

$$\mu = \bar{\mu}_{\mathrm{R}} + RT\left[\ln(1-\phi) + \phi + \chi\phi^2\right] + \frac{1}{3}\upsilon G(\alpha)\phi^{1/3}\mathbf{C}^e : \mathbf{1} - \upsilon G(\alpha)\phi + \upsilon\bar{p} \tag{46}$$

Recalling that

$$\bar{p} = -\frac{1}{3}J^{s-1}\mathbf{M}^e : \mathbf{1} = -\frac{1}{3}J^e\left(\mathbf{F}^{e\mathrm{T}}\cdot\boldsymbol{\sigma}\cdot\mathbf{F}^{e-\mathrm{T}}\right) : \mathbf{1} = -\frac{1}{3}J^e\boldsymbol{\sigma} : \mathbf{1} \tag{47}$$

and Eqs. (42), (46) can be reduced to

$$\mu = \bar{\mu}_{\mathrm{R}} + RT\left[\ln(1-\phi) + \phi + \chi\phi^2\right] - \upsilon K(\alpha)(\ln J^e)\phi \tag{48}$$

6. Numerical implementation

Recalling Eqs. (11) and (14), together with Eqs. (16) and (18) that represents the boundary value problems, and in the absence of body forces, the corresponding weak forms can be obtained by multiplying Eqs. (11) and (16) with the weighting functions $\delta\mathbf{u}$ and $\delta\mu$, respectively. Integration over the region Ω of the body yields the scalar-valued functions

$$\int_{\mathcal{B}}\left(\nabla_{\mathbf{x}}\cdot\boldsymbol{\sigma}\right)\cdot\delta\mathbf{u}\ \mathrm{d}\Omega = 0 \tag{49a}$$

$$\int_{\mathcal{B}}\left(\frac{\dot{\phi}}{J\upsilon\phi^2} - \nabla_{\mathbf{x}}\cdot\mathbf{j}\right)\delta\mu\ \mathrm{d}\Omega = 0 \tag{49b}$$

By the use of divergence theorem and accounting for the boundary conditions Eqs. (14) and (18), the weak forms can be reformulated as

$$\int_{\mathcal{B}}\left(\boldsymbol{\sigma} : \frac{\partial\delta\mathbf{u}}{\partial\mathbf{x}}\right)\ \mathrm{d}\Omega = \int_{\partial\mathcal{B}_{\mathbf{t}}}\left(\delta\mathbf{u}\cdot\bar{\mathbf{t}}\right)\ \mathrm{d}\partial\Omega \tag{50a}$$

$$\int_{\mathcal{B}}\left(\delta\mu\frac{\dot{\phi}}{J\upsilon\phi^2}\right)\ \mathrm{d}\Omega = -\int_{\mathcal{B}}\left(\frac{\partial\delta\mu}{\partial\mathbf{x}}\cdot\mathbf{j}\right)\ \mathrm{d}\Omega - \int_{\partial\mathcal{B}_{\mathbf{j}}}\left(\delta\mu\bar{j}\right)\ \mathrm{d}\partial\Omega \tag{50b}$$

Through the standard Galerkin approach (Wriggers, 2008), the displacement fields $\mathbf{u}$, the chemical potential μ, and their corresponding weighting functions $\delta\mathbf{u}$ and $\delta\mu$ can be interpolated by the shape functions N, and expressed as

$$\mathbf{u} = \sum\mathbf{u}^I N^I \quad \text{and} \quad \delta\mathbf{u} = \sum\delta\mathbf{u}^I N^I \tag{51a}$$

$$\mu = \sum\mu^I N^I \quad \text{and} \quad \delta\mu = \sum\delta\mu^I N^I \tag{51b}$$

with I and J denote the node number of the element. By substituting Eq. (51) into Eq. (50), the following system of equations in the element level read

$$\int_{\mathcal{B}^e}\left(\boldsymbol{\sigma}\cdot\frac{\partial N^I}{\partial\mathbf{x}}\right)\ \mathrm{d}\Omega = \int_{\partial\mathcal{B}^e_{\mathbf{t}}}\left(N^I\bar{\mathbf{t}}\right)\ \mathrm{d}\partial\Omega \tag{52a}$$

$$\int_{\mathcal{B}^e}\left(N^I\frac{\dot{\phi}}{J\upsilon\phi^2}\right)\ \mathrm{d}\Omega = -\int_{\mathcal{B}^e}\left(\frac{\partial N^I}{\partial\mathbf{x}}\cdot\mathbf{j}\right)\ \mathrm{d}\Omega - \int_{\partial\mathcal{B}^e_{\mathbf{j}}}\left(N^I\bar{j}\right)\ \mathrm{d}\partial\Omega \tag{52b}$$

This set of coupled equations can be solved by the iterative Newton–Raphson solution scheme by defining the following residuals for the displacement $\mathbf{u}$ and the chemical potential μ in the element level

$$\mathbf{R}^I_{\mathbf{u}} = -\int_{\mathcal{B}^e}\left(\boldsymbol{\sigma}\cdot\frac{\partial N^I}{\partial\mathbf{x}}\right)\ \mathrm{d}\Omega + \int_{\partial\mathcal{B}^e_{\mathbf{t}}}\left(N^I\bar{\mathbf{t}}\right)\ \mathrm{d}\partial\Omega \tag{53a}$$

$$R^I_{\mu} = \int_{\mathcal{B}^e}\left(N^I\frac{\dot{\phi}}{J\upsilon\phi^2}\right)\ \mathrm{d}\Omega + \int_{\mathcal{B}^e}\left(\frac{\partial N^I}{\partial\mathbf{x}}\cdot\mathbf{j}\right)\ \mathrm{d}\Omega + \int_{\partial\mathcal{B}^e_{\mathbf{j}}}\left(N^I\bar{j}\right)\ \mathrm{d}\partial\Omega \tag{53b}$$

and given the definition of solvent flux in Eq. (17), the residual equations in the index form can be written as

$$R^I_{u_i} = -\int_{\mathcal{B}^e}\left(\sigma_{ij}\frac{\partial N^I}{\partial x_j}\right)\,\mathrm{d}\Omega + \int_{\partial\mathcal{B}^e_{\mathbf{t}}}\left(N^I\bar{t}_i\right)\,\mathrm{d}\partial\Omega \tag{54a}$$

$$R^I_{\mu} = \int_{\mathcal{B}^e}\left(N^I\frac{\dot{\phi}}{J\upsilon\phi^2}\right)\,\mathrm{d}\Omega - \int_{\mathcal{B}^e}\left(m\frac{\partial N^I}{\partial x_i}\frac{\partial \mu}{\partial x_i}\right)\,\mathrm{d}\Omega + \int_{\partial\mathcal{B}^e_{\mathbf{j}}}\left(N^I\bar{j}\right)\,\mathrm{d}\partial\Omega \tag{54b}$$

The consistent linearization of the coupled polymer–solvent system in the matrix form is given by

$$\begin{bmatrix}\mathbf{K}_{\mathbf{uu}} & \mathbf{K}_{\mathbf{u}\mu}\\ \mathbf{K}_{\mu\mathbf{u}} & \mathbf{K}_{\mu\mu}\end{bmatrix}\begin{bmatrix}\Delta\mathbf{u}\\ \Delta\boldsymbol{\mu}\end{bmatrix} = -\begin{bmatrix}\mathbf{R}_{\mathbf{u}}\\ \mathbf{R}_{\mu}\end{bmatrix} \tag{55}$$

with the components of tangents corresponding to the node number I and J defined as

$$\begin{aligned}\mathbf{K}^{IJ}_{\mathbf{uu}} &= -\frac{\partial \mathbf{R}^I_{\mathbf{u}}}{\partial \mathbf{u}^J} \quad \text{and} \quad \mathbf{K}^{IJ}_{\mathbf{u}\mu} = -\frac{\partial \mathbf{R}^I_{\mathbf{u}}}{\partial \mu^J}\\ \mathbf{K}^{IJ}_{\mu\mathbf{u}} &= -\frac{\partial R^I_{\mu}}{\partial \mathbf{u}^J} \quad \text{and} \quad K^{IJ}_{\mu\mu} = -\frac{\partial R^I_{\mu}}{\partial \mu^J}\end{aligned} \tag{56}$$

For convenience, the tangent component $\mathbf{K}^{IJ}_{\mathbf{uu}}$ in index form is derived as

$$\begin{aligned}
K^{IJ}_{u_iu_k} &= -\frac{\partial R^I_{u_i}}{\partial u^J_k} = \int_{\mathcal{B}^e_0}\frac{\partial}{\partial u^J_k}\left(J\sigma_{ij}\frac{\partial N^I}{\partial x_j}\right)\,\mathrm{d}\Omega_{\mathrm{R}} - \int_{\partial\mathcal{B}^e_{\mathbf{t}}} N^IN^J\frac{\partial \bar{t}_i}{\partial u_k}\,\mathrm{d}\partial\Omega\\
&= \int_{\mathcal{B}^e_0}\frac{\partial}{\partial u^J_k}\left(\tau_{ij}\frac{\partial N^I}{\partial X_a}F^{-1}_{aj}\right)\,\mathrm{d}\Omega_{\mathrm{R}} - \int_{\partial\mathcal{B}^e_{\mathbf{t}}} N^IN^J\frac{\partial \bar{t}_i}{\partial u_k}\,\mathrm{d}\partial\Omega\\
&= \int_{\mathcal{B}^e_0}\frac{\partial N^I}{\partial X_a}\left(\frac{\partial F^{-1}_{aj}}{\partial F_{mn}}\tau_{ij} + F^{-1}_{aj}\frac{\partial \tau_{ij}}{\partial F_{mn}}\right)\frac{\partial F_{mn}}{\partial u^J_k}\,\mathrm{d}\Omega_{\mathrm{R}} - \int_{\partial\mathcal{B}^e_{\mathbf{t}}} N^IN^J\frac{\partial \bar{t}_i}{\partial u_k}\,\mathrm{d}\partial\Omega\\
&= \int_{\mathcal{B}^e_0}\frac{\partial N^I}{\partial X_a}\left(-F^{-1}_{nj}F^{-1}_{am}\tau_{ij} + F^{-1}_{aj}\frac{\partial \tau_{ij}}{\partial F_{mn}}\right)\frac{\partial N^J}{\partial X_n}\delta_{mk}\,\mathrm{d}\Omega_{\mathrm{R}} - \int_{\partial\mathcal{B}^e_{\mathbf{t}}} N^IN^J\frac{\partial \bar{t}_i}{\partial u_k}\,\mathrm{d}\partial\Omega\\
&= \int_{\mathcal{B}^e_0}\frac{\partial N^I}{\partial X_a}\left(-F^{-1}_{ak}F^{-1}_{nj}\tau_{ij} + F^{-1}_{aj}\frac{\partial \tau_{ij}}{\partial F_{kn}}\right)\frac{\partial N^J}{\partial X_n}\,\mathrm{d}\Omega_{\mathrm{R}} - \int_{\partial\mathcal{B}^e_{\mathbf{t}}} N^IN^J\frac{\partial \bar{t}_i}{\partial u_k}\,\mathrm{d}\partial\Omega\\
&= \int_{\mathcal{B}^e_0}\frac{\partial N^I}{\partial x_r}F_{ra}\left(-F^{-1}_{ak}F^{-1}_{nj}\tau_{ij} + F^{-1}_{aj}\frac{\partial \tau_{ij}}{\partial F_{kn}}\right)F_{ln}\frac{\partial N^J}{\partial x_l}\,\mathrm{d}\Omega_{\mathrm{R}} - \int_{\partial\mathcal{B}^e_{\mathbf{t}}} N^IN^J\frac{\partial \bar{t}_i}{\partial u_k}\,\mathrm{d}\partial\Omega\\
&= \int_{\mathcal{B}^e_0}\frac{\partial N^I}{\partial x_r}\left(-\delta_{rk}\tau_{il} + F_{ln}\frac{\partial \tau_{ir}}{\partial F_{kn}}\right)\frac{\partial N^J}{\partial x_l}\,\mathrm{d}\Omega_{\mathrm{R}} - \int_{\partial\mathcal{B}^e_{\mathbf{t}}} N^IN^J\frac{\partial \bar{t}_i}{\partial u_k}\,\mathrm{d}\partial\Omega\\
&= \int_{\mathcal{B}^e}\frac{\partial N^I}{\partial x_r}\left(-J^{-1}\delta_{rk}\tau_{il} + J^{-1}F_{ln}\frac{\partial \tau_{ir}}{\partial F_{kn}}\right)\frac{\partial N^J}{\partial x_l}\,\mathrm{d}\Omega - \int_{\partial\mathcal{B}^e_{\mathbf{t}}} N^IN^J\frac{\partial \bar{t}_i}{\partial u_k}\,\mathrm{d}\partial\Omega\\
&= \int_{\mathcal{B}^e}\frac{\partial N^I}{\partial x_r}\left(-J^{-1}\delta_{rk}\tau_{il} + J^{-1}F_{ln}F_{rm}\frac{\partial P_{im}}{\partial F_{kn}} + J^{-1}\delta_{rk}\tau_{il}\right)\frac{\partial N^J}{\partial x_l}\,\mathrm{d}\Omega - \int_{\partial\mathcal{B}^e_{\mathbf{t}}} N^IN^J\frac{\partial \bar{t}_i}{\partial u_k}\,\mathrm{d}\partial\Omega\\
&= \int_{\mathcal{B}^e}\frac{\partial N^I}{\partial x_r}\left(J^{-1}F_{ln}F_{rm}\frac{\partial P_{im}}{\partial F_{kn}}\right)\frac{\partial N^J}{\partial x_l}\,\mathrm{d}\Omega - \int_{\partial\mathcal{B}^e_{\mathbf{t}}} N^IN^J\frac{\partial \bar{t}_i}{\partial u_k}\,\mathrm{d}\partial\Omega
\end{aligned} \tag{57}$$

with

$$\begin{aligned}
\frac{\partial P_{im}}{\partial F_{kn}} &= \frac{\partial}{\partial F_{kn}}\left[G(\alpha)\left(F_{im} - F^{-1}_{mi}\right) + K(\alpha)(\ln J^e)F^{-1}_{mi}\right]\\
&= G(\alpha)\delta_{ik}\delta_{mn} - G(\alpha)\frac{\partial F^{-1}_{mi}}{\partial F_{kn}} + K(\alpha)F^{-1}_{mi}\frac{\partial(\ln J^e)}{\partial F_{kn}} + K(\alpha)(\ln J^e)\frac{\partial F^{-1}_{mi}}{\partial F_{kn}}\\
&= G(\alpha)\delta_{ik}\delta_{mn} + G(\alpha)F^{-1}_{ni}F^{-1}_{mk} + K(\alpha)F^{-1}_{mi}\frac{\partial(\ln J^e)}{\partial F_{kn}} - K(\alpha)(\ln J^e)F^{-1}_{ni}F^{-1}_{mk}\\
&= G(\alpha)\delta_{ik}\delta_{mn} + G(\alpha)F^{-1}_{ni}F^{-1}_{mk} + K(\alpha)F^{-1}_{mi}\frac{\partial(\ln \phi J)}{\partial F_{kn}} - K(\alpha)(\ln J^e)F^{-1}_{ni}F^{-1}_{mk}\\
&= G(\alpha)\left(\delta_{ik}\delta_{mn} + F^{-1}_{ni}F^{-1}_{mk}\right) + K(\alpha)\left[F^{-1}_{mi}F^{-1}_{nk} - (\ln J^e)F^{-1}_{ni}F^{-1}_{mk}\right]
\end{aligned} \tag{58}$$

Next, recalling Eqs. (44) and (48), the tangent $\mathbf{K}^{IJ}_{\mathbf{u}\mu}$ in index form is given by

$$\begin{aligned}
K^{IJ}_{u_i\mu} &= -\frac{\partial R^I_{u_i}}{\partial \mu^J} = \int_{\mathcal{B}^e}\frac{\partial N^I}{\partial x_j}\left(\frac{\sigma_{ij}}{\partial\phi}\frac{\partial\phi}{\partial\mu}\right)N^J\,\mathrm{d}\Omega\\
&= \int_{\mathcal{B}^e}\frac{\partial N^I}{\partial x_j}\frac{K(\alpha)}{J\phi}\delta_{ij}\left(\frac{\partial\mu}{\partial\phi}\right)^{-1}N^J\,\mathrm{d}\Omega
\end{aligned} \tag{59}$$

Then the tangent $\mathbf{K}^{IJ}_{\mu\mathbf{u}}$ in index form can be derived as

$$
\begin{aligned}
K^{IJ}_{\mu u_k} &= -\frac{\partial R^I_{u_i}}{\partial u^J_k} = \frac{\partial}{\partial u^J_k}\left(\int_{\mathcal{B}^e} m\frac{\partial N^I}{\partial x_i}\frac{\partial \mu}{\partial x_i}\,\mathrm{d}\Omega\right)\\
&= \frac{\partial}{\partial u^J_k}\left(\int_{\mathcal{B}^e_0} mJ\frac{\partial N^I}{\partial X_a}F^{-1}_{ai}\frac{\partial \mu}{\partial X_b}F^{-1}_{bi}\,\mathrm{d}\Omega_{\mathrm{R}}\right)\\
&= \int_{\mathcal{B}^e_0} m\frac{\partial N^I}{\partial X_a}\frac{\partial \mu}{\partial X_b}\frac{\partial\left(JF^{-1}_{ai}F^{-1}_{bi}\right)}{\partial u^J_k}\,\mathrm{d}\Omega_{\mathrm{R}}\\
&= \int_{\mathcal{B}^e_0} m\frac{\partial N^I}{\partial X_a}\frac{\partial \mu}{\partial X_b}\frac{\partial\left(JF^{-1}_{ai}F^{-1}_{bi}\right)}{\partial F_{mn}}\frac{\partial F_{mn}}{\partial u^J_k}\,\mathrm{d}\Omega_{\mathrm{R}}\\
&= \int_{\mathcal{B}^e_0} m\frac{\partial N^I}{\partial X_a}\frac{\partial \mu}{\partial X_b}\left(JF^{-1}_{nm}F^{-1}_{ai}F^{-1}_{bi} - JF^{-1}_{am}F^{-1}_{ni}F^{-1}_{bi} - JF^{-1}_{ai}F^{-1}_{bm}F^{-1}_{ni}\right)\frac{\partial F_{mn}}{\partial u^J_k}\,\mathrm{d}\Omega_{\mathrm{R}}\\
&= \int_{\mathcal{B}^e} m\frac{\partial N^I}{\partial X_a}\frac{\partial \mu}{\partial X_b}\left(F^{-1}_{nm}F^{-1}_{ai}F^{-1}_{bi} - F^{-1}_{am}F^{-1}_{ni}F^{-1}_{bi} - F^{-1}_{ai}F^{-1}_{bm}F^{-1}_{ni}\right)\frac{\partial N^J}{\partial X_n}\delta_{mk}\,\mathrm{d}\Omega\\
&= \int_{\mathcal{B}^e} m\frac{\partial N^I}{\partial X_a}\frac{\partial \mu}{\partial X_b}\left(F^{-1}_{nk}F^{-1}_{ai}F^{-1}_{bi} - F^{-1}_{ak}F^{-1}_{ni}F^{-1}_{bi} - F^{-1}_{ai}F^{-1}_{bk}F^{-1}_{ni}\right)\frac{\partial N^J}{\partial X_n}\,\mathrm{d}\Omega\\
&= \int_{\mathcal{B}^e} m\left(\frac{\partial N^I}{\partial x_i}\frac{\partial \mu}{\partial x_i}\frac{\partial N^J}{\partial x_k} - \frac{\partial N^I}{\partial x_k}\frac{\partial \mu}{\partial x_i}\frac{\partial N^J}{\partial x_i} - \frac{\partial N^I}{\partial x_i}\frac{\partial \mu}{\partial x_k}\frac{\partial N^J}{\partial x_i}\right)\mathrm{d}\Omega\\
&= \int_{\mathcal{B}^e} m\frac{\partial N^I}{\partial x_i}\left(\delta_{jk}\frac{\partial \mu}{\partial x_i} - \delta_{ik}\frac{\partial \mu}{\partial x_j} - \delta_{ij}\frac{\partial \mu}{\partial x_k}\right)\frac{\partial N^J}{\partial x_j}\,\mathrm{d}\Omega
\end{aligned}
\tag{60}
$$

Similarly, the last tangent $K^{IJ}_{\mu\mu}$ is given by

$$
\begin{aligned}
K^{IJ}_{\mu\mu} &= -\frac{\partial R^I_{\mu}}{\partial \mu^J} = \frac{\partial}{\partial \mu^J}\left[\int_{\mathcal{B}^e}\left(-N^I\frac{\dot{\phi}}{J\upsilon\phi^2} + m\frac{\partial N^I}{\partial x_i}\frac{\partial \mu}{\partial x_i}\right)\mathrm{d}\Omega - \int_{\partial\mathcal{B}^e_{\mathbf{j}}}\left(N^I\bar{j}\right)\,\mathrm{d}\partial\Omega\right]\\
&= -\int_{\mathcal{B}^e}\frac{N^I}{J\upsilon}\frac{\partial}{\partial \mu^J}\left(\frac{\dot{\phi}}{\phi^2}\right)\mathrm{d}\Omega + \int_{\mathcal{B}^e}\frac{\partial N^I}{\partial x_i}\frac{\partial}{\partial \mu^J}\left(m\frac{\partial \mu}{\partial x_i}\right)\mathrm{d}\Omega - \int_{\partial\mathcal{B}^e_{\mathbf{j}}} N^I\frac{\partial \bar{j}}{\partial \mu^J}\,\mathrm{d}\partial\Omega\\
&= -\int_{\mathcal{B}^e}\frac{N^I}{J\upsilon}\left(-2\frac{\dot{\phi}}{\phi^3}\frac{\partial \phi}{\partial \mu^J} + \frac{1}{\phi^2}\frac{\partial \dot{\phi}}{\partial \mu^J}\right)\mathrm{d}\Omega + \int_{\mathcal{B}^e}\frac{\partial N^I}{\partial x_i}\frac{\partial m}{\partial \mu^J}\frac{\partial \mu}{\partial x_i}\,\mathrm{d}\Omega\\
&\quad + \int_{\mathcal{B}^e} m\frac{\partial N^I}{\partial x_i}\frac{\partial N^J}{\partial x_i}\,\mathrm{d}\Omega - \int_{\partial\mathcal{B}^e_{\mathbf{j}}}\left(N^IN^J\frac{\partial \bar{j}}{\partial \mu}\right)\mathrm{d}\partial\Omega\\
&= -\int_{\mathcal{B}^e}\frac{N^IN^J}{J\upsilon\phi^2}\left(-2\frac{\dot{\phi}}{\phi}\frac{\partial \phi}{\partial \mu} + \frac{\partial \dot{\phi}}{\partial \mu}\right)\mathrm{d}\Omega + \int_{\mathcal{B}^e}\frac{\partial N^I}{\partial x_i}N^J\frac{\partial m}{\partial \mu}\frac{\partial \mu}{\partial x_i}\,\mathrm{d}\Omega\\
&\quad + \int_{\mathcal{B}^e} m\frac{\partial N^I}{\partial x_i}\frac{\partial N^J}{\partial x_i}\,\mathrm{d}\Omega - \int_{\partial\mathcal{B}^e_{\mathbf{j}}}\left(N^IN^J\frac{\partial \bar{j}}{\partial \mu}\right)\mathrm{d}\partial\Omega\\
&= -\int_{\mathcal{B}^e}\frac{N^IN^J}{J\upsilon\phi^2}\left[-2\frac{\dot{\phi}}{\phi}\left(\frac{\partial \mu}{\partial \phi}\right)^{-1} + \frac{\partial \dot{\phi}}{\partial \mu}\right]\mathrm{d}\Omega + \int_{\mathcal{B}^e}\frac{\partial N^I}{\partial x_i}N^J\frac{\partial m}{\partial \phi}\left(\frac{\partial \mu}{\partial \phi}\right)^{-1}\frac{\partial \mu}{\partial x_i}\,\mathrm{d}\Omega\\
&\quad + \int_{\mathcal{B}^e} m\frac{\partial N^I}{\partial x_i}\frac{\partial N^J}{\partial x_i}\,\mathrm{d}\Omega - \int_{\partial\mathcal{B}^e_{\mathbf{j}}}\left(N^IN^J\frac{\partial \bar{j}}{\partial \mu}\right)\mathrm{d}\partial\Omega
\end{aligned}
\tag{61}
$$

Notably, by the use of Eq. (48) and $J^e = J\phi$, the polymer volume fraction ϕ in the numerical solution is determined explicitly from the following nonlinear equation

$$
\frac{\bar{\mu}_{\mathrm{R}} - \mu}{RT} + \ln(1-\phi) + \phi + \chi\phi^2 - \frac{\upsilon K(\alpha)}{RT}\ln(J\phi)\phi = 0 \tag{62}
$$

Besides, its rate $\dot{\phi}$ is calculated through the difference approximation

$$
\dot{\phi} = \frac{\phi_{n+1} - \phi_n}{\Delta t} \tag{63}
$$

where ϕ_{n+1} and ϕ_n denote the values of polymer volume fraction at the current and previous time increments, respectively. The computational framework is implemented into the finite element program Abaqus, and convergence is accepted if both the largest residual and correction to the solution are less than the prescribed tolerance values at each time increment.

7. Numerical application to PV recycling

In this section, the coupled chemo-mechanical responses of EVA copolymer with application to the recycling of end-of-life photovoltaic modules using the organic solvent method are simulated to illustrate the capability of the computational framework.

Table 1
Model parameters of EVA copolymer for the coupled modeling.

Parameter	Value
G^0 (298 K)	5 MPa (Badiee, Ashcroft, & Wildman, 2016)
G^1 (298 K)	20 MPa
ν	0.495 (Badiee et al., 2016)
χ_S	0.34 (Díez et al., 2014)
δ_p	17.5 $MPa^{1/2}$ (Díez et al., 2014)
γ	100

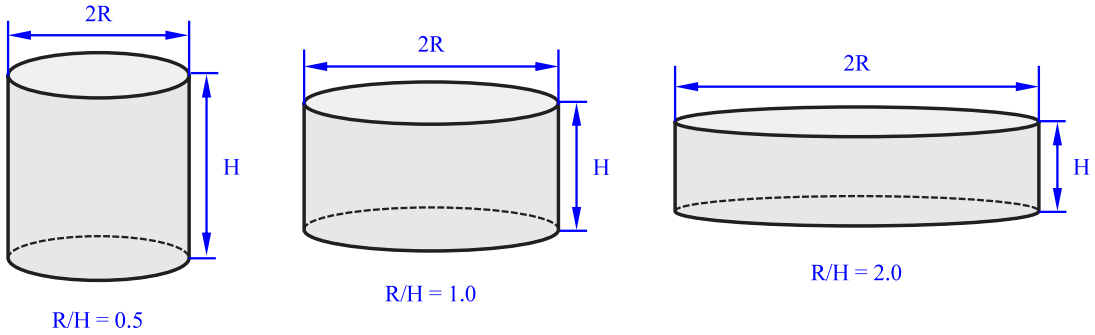

Fig. 2. Cylindrical EVA samples with three different aspect ratios (0.5, 1.0, and 2.0) between radius and height.

The first case is the numerical simulation of the free-swelling experiments of cylindrical EVA samples with different types of solvents (Toluene, Tetrahydrofuran, and Octane), and subsequent comparison with available testing data is addressed for validation purposes. It should be pointed out that these solvents have been chosen because they cannot dissolve the EVA copolymer at the particular temperatures but cause swelling when coming into contact (Mencer & Gomzi, 1994). Then the second case demonstrates the capability of this computational framework to model the effects of initial crosslinking and mechanical constraints on the time history evolution of complex coupled response. Finally, since the cracking of silicon solar cells due to EVA swelling is the critical problem in PV recyling using the solvent method (Doi et al., 2001), the complete PV laminate is modeled in the 3D setting to study the deformation and diffusion mechanisms, and the mechanical and swelling responses under different conditions are analyzed in detail. Based on the well-established experimental evidence in the literature, the basic model parameters associated with the properties of EVA copolymer are listed in Table 1. The initial chemical potential of dry EVA polymer is defined by Eq. (48) with the reference chemical potential of the solvent $\bar{\mu}_R$ equal to 0.0 J/mol, and the default initial crosslinking degree is set to 0.0 unless specified in the following. It should be pointed out that the value of polymer volume fraction ϕ at time 0.0 is set to 0.999 rather than 1.0 to avoid numerical difficulties. For convenience, the swelling degree is specified as the ratio between the solvent volume and total volume of both solvent and EVA polymer (Mencer & Gomzi, 1994).

7.1. Swelling simulation of cylindrical EVA samples

In this example, the transient free swelling of cylindrical EVA samples with different types of solvents is simulated according to the experiments (Mencer & Gomzi, 1994). To study the swelling kinetics of EVA polymer in different solvents, the apparatus consisting of two round reservoirs connecting to each other with a graduated tube was designed to perform the experiments as reported in Mencer and Gomzi (1994). Before testing, the solvent level in the tube was recorded when the apparatus was vertical and there was no contact between solvent and the dry EVA polymer samples. On turning the apparatus to the horizontal state, the solvent penetrated into the specimen and the kinematic measurements started. After certain time periods, the apparatus was turned back to the vertical state and the solvent level in the graduated tube was recorded again. In this way, the volume decrease of solvent level is equal to the volume increase of the polymer specimen. The initial volume of the specimen is 0.15 cm^3, but the shape is not mentioned in Mencer and Gomzi (1994). To investigate this influence, cylindrical specimens with three different aspect ratios between radius and height (0.5, 1.0, and 2.0) are chosen in the following simulation, see Fig. 2. The isothermal condition with the constant temperature of 298 K is assumed in this work. Three different solvents including Toluene, Tetrahydrofuran, and Octane are considered, and their basic properties are reported in Table 2. Due to symmetry, only a half of axisymmetric cylindrical slice is modeled to save computational cost. Zero chemical potential boundary condition is prescribed on the outer surfaces of specimen.

The contour plots of polymer volume fraction ϕ for the three cylindrical models with different ratios between the radius and height obtained from simulation after 15 min, 30 min, and 45 min in the solvent of Tetrahydrofuran are shown in Fig. 3. Note that as the solvent penetrates into the EVA copolymer, the volumes of models change with time for all the three different shapes. The EVA models gradually increases their volumes because of the entry of solvent molecules and subsequent combination with the polymer molecules by physical forces. This swelling phenomena can be ascribed to the higher interaction energy between the polymer molecules than that for their interaction with solvent molecules at this temperature condition of 298 K. Besides, it should

Table 2
Solvent properties for the swelling simulation (Mencer & Gomzi, 1994; Padhi, Raju Achary, & Nayak, 2015).

	Toluene	Tetrahydrofuran	Octane
υ (m^3/mol)	1.068×10^{-4}	7.79×10^{-5}	1.635×10^{-4}
D (m^2/s)	4.04×10^{-11}	4.0×10^{-11}	4.0×10^{-11}
$\delta_{s,d}$ ($MPa^{1/2}$)	18.0	16.8	15.6
$\delta_{s,p}$ ($MPa^{1/2}$)	1.4	5.7	0.0
$\delta_{s,h}$ ($MPa^{1/2}$)	2.0	8.0	0.0

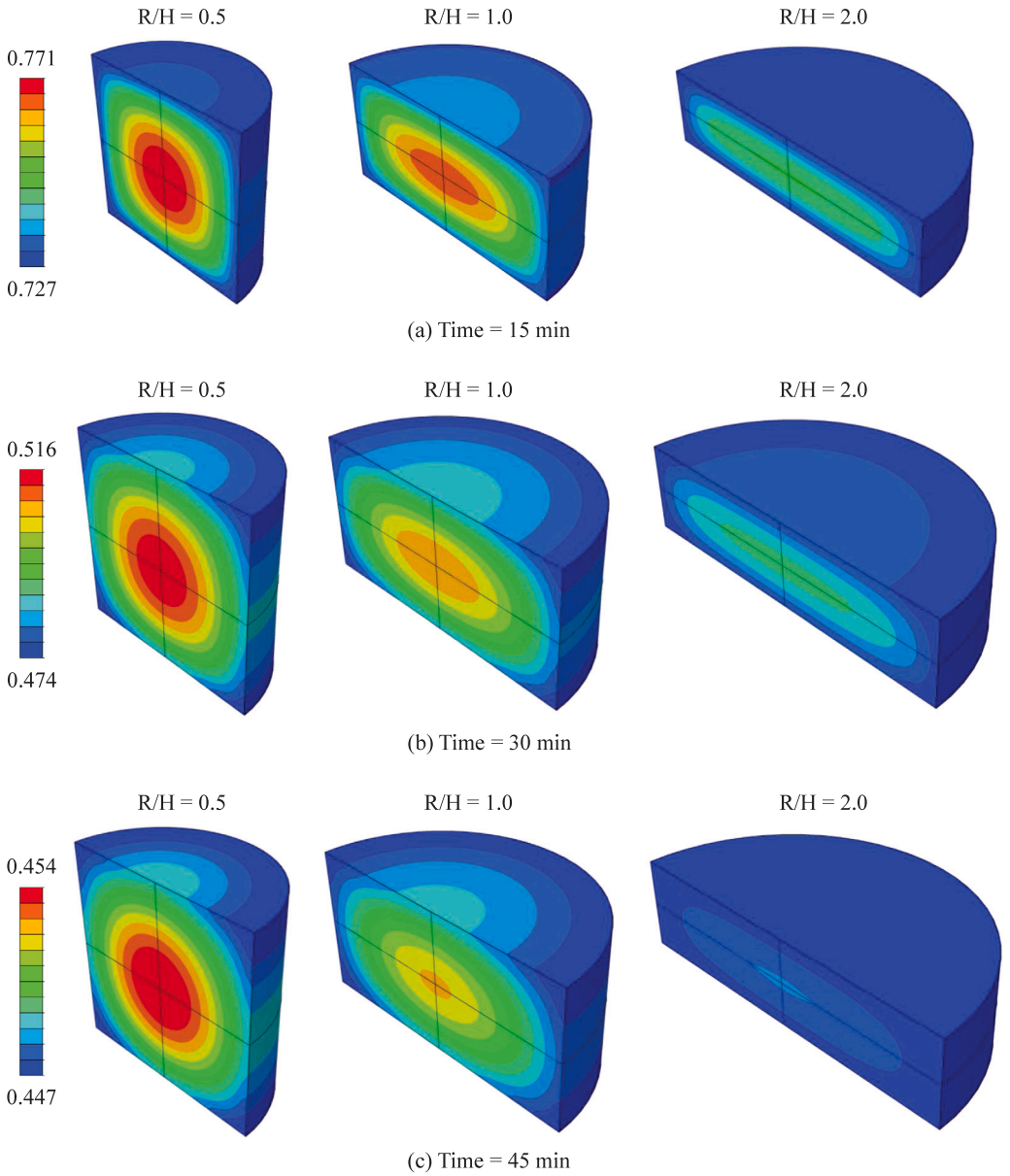

Fig. 3. Comparison of the contour plots of the polymer volume fraction in Tetrahydrofuran after (a) 15 min, (b) 30 min, and (c) 45 min for the three different models with the ratio between radius and height equal to 0.5, 1.0, and 2.0.

be pointed out that the volume change process is not only the absorption and diffusion of solvent molecules but also the change in polymer structure of the EVA. As mentioned in Mencer and Gomzi (1994), on the one hand, as solvent molecules penetrate into the interstructural space between polymer molecules, the supermolecular polymer structures are formed, which results into the interstructural swelling. On the other hand, the solvent molecules will also penetrate into the internal polymer molecule structures,

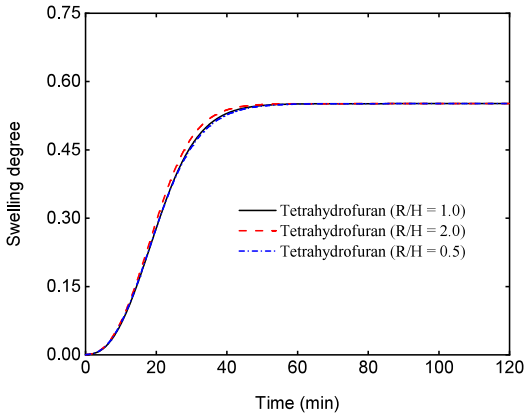

Fig. 4. The time history plots of swelling degree in Tetrahydrofuran for the three different models with the ratio between radius and height equal to 1.0, 0.5, and 2.0.

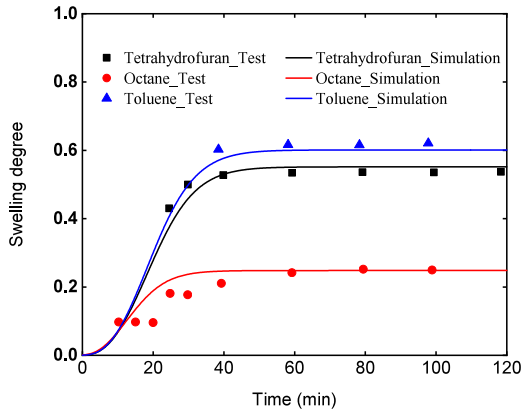

Fig. 5. Comparison of the time history curves of swelling degree in the three different solvents between experiments and numerical simulation.

leading to the so-called intrastructural swelling. From the sectional view of the cylindrical models in Fig. 3, it is also clearly observed that the polymer volume fraction ϕ increases from the boundary to the inside portion of EVA, which represents the solvent diffusion as well as the polymer swelling process. To better quantify the effects of ratio between radius and height, the time history responses of swelling degree for three different models in the solvent of Tetrahydrofuran are shown in Fig. 4. Generally, the time history curves of swelling degree for the three different models agree with each other very well, which indicates that the ratio between the radius and height has no significant influence on the swelling behavior of the EVA copolymer in solvents under the isothermal condition. In the remaining part of this section, only the cylindrical model with the ratio between the radius and height equal to 1.0 will be considered.

The swelling phenomena in the EVA polymer–solvent system is mainly caused by the interactions due to the dispersive forces, but the solvent properties such as the molar volume and viscosity also greatly influence the kinetics. In the following, three solvents (Toluene, Tetrahydrofuran, and Octane) with different basic properties have been chosen in the numerical simulation of swelling tests of EVA samples with the cylindrical shape at the constant temperature of 298 K reported in Mencer and Gomzi (1994). The comparison of time history curves of swelling degree in the three different solvents between simulation and experiments are shown in Fig. 5. The swelling degree changed over time, and the volume change lasted until the equilibrium state when the swelling degree became constant. Also note that the same polymer reaches the different equilibrium swelling degrees in the three solvents due to the different molar volumes and viscosity parameters. Compared with the swelling behavior of polymer samples in Tetrahydrofuran and Toluene, the corresponding equilibrium swelling degree in Octane is significantly lower because of its lower solubility parameter. As for the cases in Toluene and Tetrahydrofuran, not much difference of equilibrium swelling degree can be observed as a result of approximately equal Flory–Huggins parameter determined by the corresponding solvent properties. The swelling kinetics for EVA copolymer in the three solvents of different nature with respect to their interactions can be well predicted by the modeling method, and as shown in Fig. 5, the swelling time history curves obtained from simulation agree with the experimental data very well.

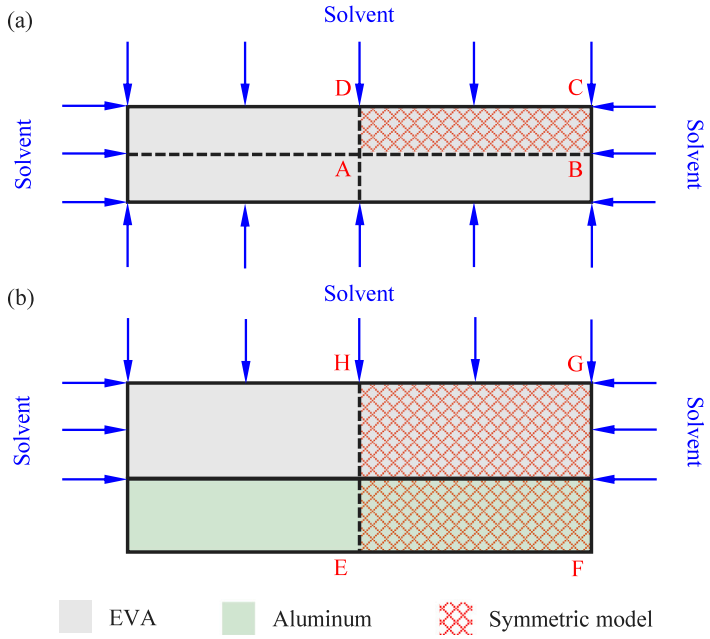

Fig. 6. Schematic for the transient swelling of (a) pure EVA sample and (b) EVA/aluminum laminate.

7.2. Effects of crosslinking and mechanical constraints

In this section, the influences of crosslinking treatment and mechanical constraints on the coupled responses of EVA polymer in PV recycling using the organic solvent method have been investigated in detail to further demonstrate the capability of the modeling framework. As mentioned in Czanderna and Pern (1996), the crosslinking process of EVA copolymer is indeed the formation of 3D polymer network that increases the stability of the elastomeric material. In this process, the hydrogen from terminal methyl groups of the EVA chains is abstracted by the cleaved radical species, and at the same time, the active radical site is transferred to the methyl group of EVA, which then creates the bond between the EVA chains through reaction. In PV lamination, the crosslinking reaction is basically the result of thermolysis at the temperature condition around 150 °C (Hirschl et al., 2013). It has shown by chemical assessment in Lange, Luo, Polo, and Zahnd (2011) that the crosslinking degree is strongly affected by both the temperature condition and lamination time during the manufacturing process. The initial crosslinking degree is considered here as a key parameter to the coupled chemo-mechanical response of the polymer–solvent system in PV recycling. In line with the tests reported in Doi et al. (2001), both the pure EVA samples and samples bonded with aluminum plate have been taken into account in the simulation to study the mixing effects. As shown in Fig. 6, due to the symmetry, only a quarter of the pure EVA sample and a half of the EVA/laminate are modeled in the plane strain condition. The width and thickness of the EVA sample are 15 mm and 3 mm, respectively. For the elastic modeling of aluminum substrate using the Kirchhoff–Saint-Venant constitutive model, the Young's modulus and Poisson ratio are set to 69 GPa and 0.33, respectively, which are taken from Lee and Tay (2013). In the first case of pure EVA sample, symmetric boundary conditions are imposed on the edges AB and AD, while in the second case of EVA/aluminum laminate, the symmetric boundary condition is applied to the edge EH. The solvent can penetrate into the two symmetric models from the edges BC, CD, GH, and part of edge FG that belongs to EVA, and the other edges are prescribed to zero-flux chemical boundary conditions.

The contour plots of polymer volume fraction ϕ of the pure EVA samples with the crosslinking degree $\alpha = 0.0$ and $\alpha = 1.0$ at 15 min, 30 min, and 45 min are shown in Fig. 7. It can be clearly seen the rectangular pure EVA samples in the plane strain condition gradually increase its volume over time due to the penetration of solvent. The polymer volume fraction ϕ is higher in the area close to the edges than that in the middle areas as a result of the solvent diffusion. Also, the polymer volume fraction distribution in the EVA sample becomes lower with time for both the initial crosslinking degree $\alpha = 0.0$ and $\alpha = 1.0$. On the other hand, the contour plots of polymer volume fraction ϕ of the EVA/aluminum laminate samples with the crosslinking degree $\alpha = 0.0$ and $\alpha = 1.0$ at 15 min, 30 min, and 45 min are shown in Fig. 8. As in the previous case study of pure EVA samples, the volume of EVA in the laminate structure becomes bigger over time for both two crosslinking degrees. However, the EVA body can only change along the thickness direction in this case as the bottom edges are constrained by the aluminum substrate along the horizontal direction. Note that the difference between the predictions of EVA with two crosslinking degree is intensified compared with the previous case, which can be ascribed to the coupled diffusion-deformation in the presence of mechanical constraint from the aluminum substrate. Besides, it can also be seen from Fig. 8 that the EVA part of laminate sample with no initial crosslinking cannot maintain the rectangular shape with time because of the enhanced solvent flux from the two upper corners and faster diffusion process than that with the initial crosslinking $\alpha = 1.0$. The quantitative comparison of swelling degree between the pure EVA sample and

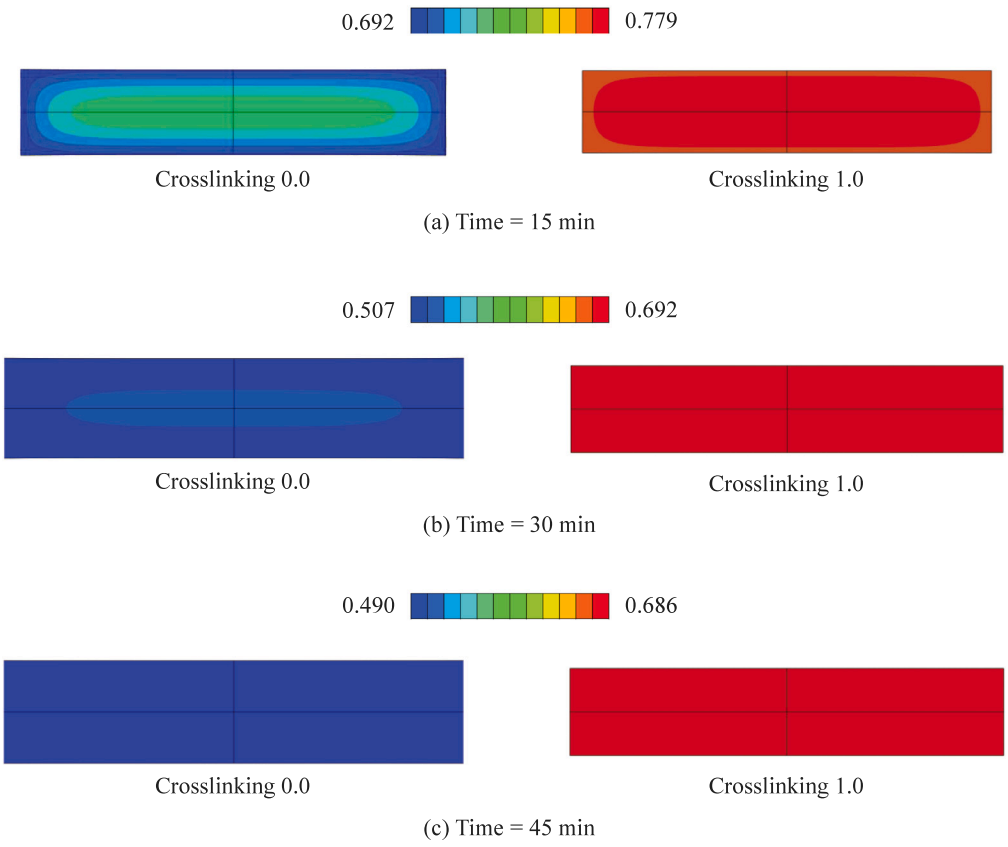

Fig. 7. Comparison of the contour plots of the polymer volume fraction at (a) 15 min, (b) 30 min, and (c) 45 min between the pure EVA samples with crosslinking degree $\alpha = 0.0$ and $\alpha = 1.0$.

EVA/aluminum laminate with two different initial crosslinking degree is shown in Fig. 9. The equilibrium swelling degree for both the pure EVA and EVA/aluminum laminate with no initial crosslinking is larger than that with initial crosslinking $\alpha = 1.0$ - this is because crosslinking can suppress the swelling behavior of EVA due to part of its dissolution. It is also worth noting that the mechanical constraint directly influence the magnitude of equilibrium swelling degree, reducing from 0.5 to 0.385 with the initial crosslinking $\alpha = 0.0$ and from 0.31 to 0.225 with the initial crosslinking $\alpha = 1.0$.

7.3. Coupled modeling of PV recycling

This section addresses the numerical simulation of the recycling of complete PV laminate using the organic solvent method under gentle temperature condition. As pointed out in Doi et al. (2001), the key problem in this recycling method is the cracking of PV silicon cells due to the swelling of EVA layers induced by solvent penetration. The characteristics of recycled intact silicon cells are of great importance to the high-value reuse and reduction of production cost. Hence, it is crucial to develop a reliable modeling framework to understand the coupled responses of EVA in different solvents during the PV recycling process. The sectional sketch of the PV laminate in the recycling process is shown in Fig. 10. A quarter of the complete PV laminate is modeled in the 3D setting to study the EVA swelling-induced deformation of silicon cells, as shown in Fig. 11. The thickness values of glass, EVA (no crosslinking), silicon cell, and backsheet are 4 mm, 0.5 mm, 0.166 mm, and 0.1 mm, respectively. Only elastic deformation is taken into account for the modeling of glass, silicon cell, and backsheet layers using the Kirchhoff–Saint-Venant constitutive model, and the basic mechanical properties are listed in Table 3. The zero chemical potential is prescribed on the outer surfaces of two EVA layers, and the initial potential for the dry EVA polymer is determined in the same way as in the previous two cases. Symmetric displacement boundary conditions are imposed on the symmetric planes, and the bottom surface of glass layer is constrained to remove rigid body motions.

The contour plots of polymer volume fraction ϕ of the first EVA layer (EVA1) in the three different solvents Toluene, Tetrahydrofuran, and Octane after 5 h, 10 h, and 15 h are shown in Fig. 12. At each of the three different time points, the polymer volume fraction of the first EVA layer (EVA1) in Toluene is lower than that in the other two solvents Tetrahydrofuran and Octane, which is mainly because of the high molar volume and viscosity of Toluene. The polymer volume fraction values of EVA1 at equilibrium in Toluene, Tetrahydrofuran, and Octane are approximately 0.587, 0.612, and 0.780, respectively. After 15 h,

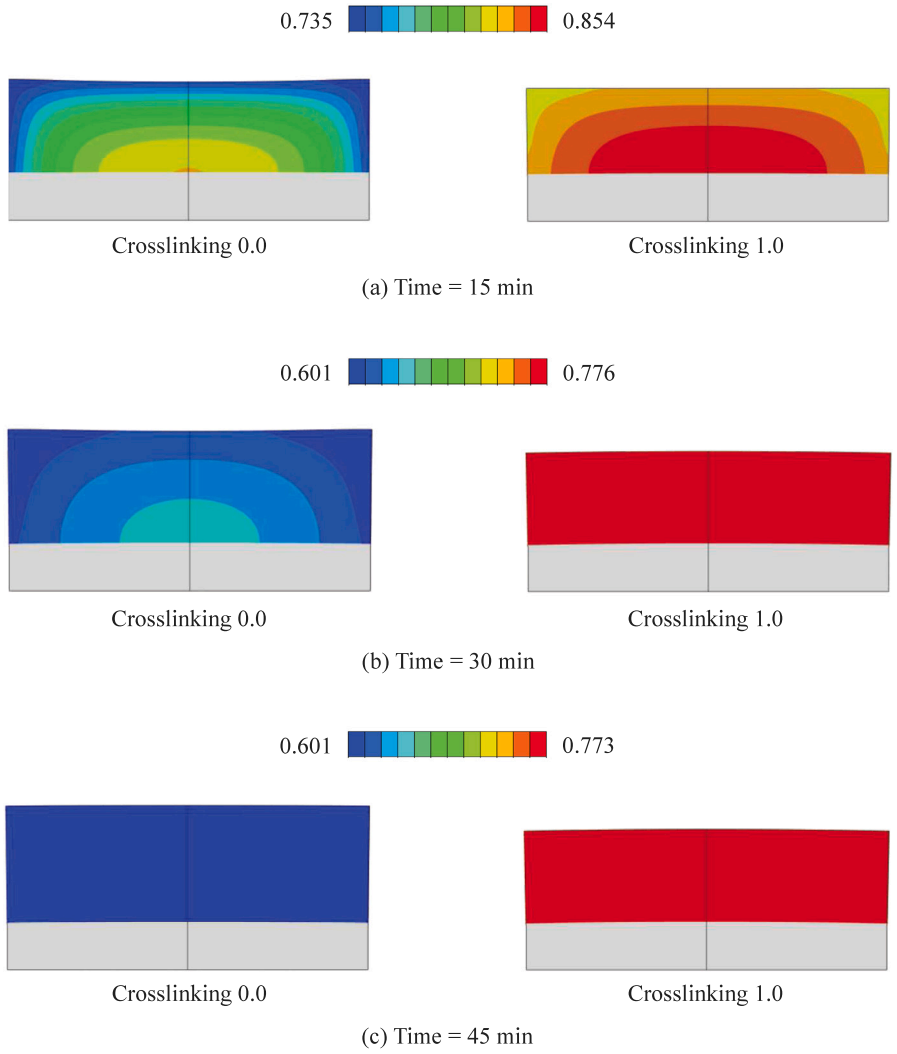

Fig. 8. Comparison of the contour plots of the polymer volume fraction at (a) 15 min, (b) 30 min, and (c) 45 min between the EVA/aluminum laminate samples with crosslinking degree $\alpha = 0.0$ and $\alpha = 1.0$ (aluminum in gray color).

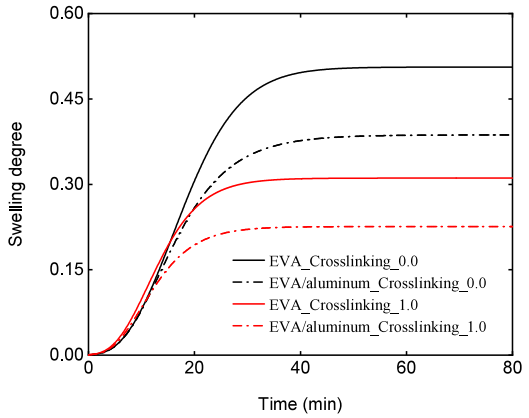

Fig. 9. Comparison of the time history curves of swelling degree between the pure EVA samples and EVA/aluminum laminates with crosslinking degree $\alpha = 0.0$ and $\alpha = 1.0$.

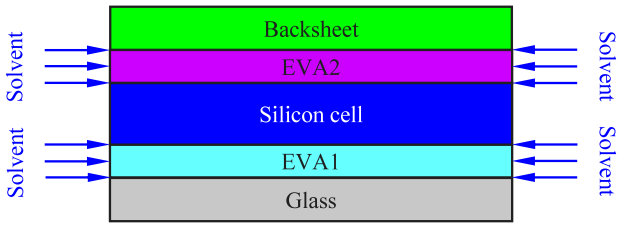

Fig. 10. The sectional sketch of the PV module in the recycling process.

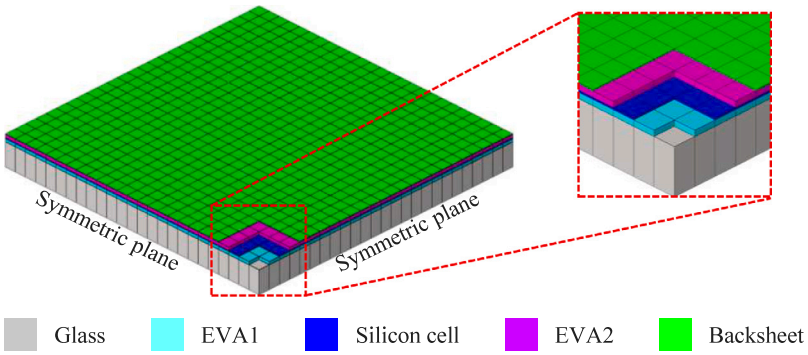

Fig. 11. Finite element model of a quarter of the complete PV laminate.

Table 3
Mechanical properties for PV modules (Corrado, Infuso, & Paggi, 2017; Paggi, Kajari-Schröder, & Eitner, 2011).

	E (GPa)	Density (kg/m^3)	ν
Backsheet	2.8	1200	0.3
Silicon	130	2329	0.2
Glass	73	2500	0.24

the polymer volume fraction value in the middle area of EVA1 in Octane is the highest among the three cases, which can be ascribed to the lowest Flory–Huggins parameter. The spatial variation of the polymer volume fraction ϕ of the first EVA layer in the three different solvents after 1 h, 5 h, 10 h, and 15 h are shown in Fig. 13. At 1 h, the polymer volume fraction at the central area remains the value of 1.0 due to the lack of solvent penetration. No significant difference of the spatial distribution of polymer volume fraction in the solvents Tetrahydrofuran and Toluene can be observed at this time point because of their similar solubility parameters. After 15 h, it can be clearly seen from Fig. 13(d) that the polymer volume fraction distribution plot of EVA1 in Octane is much higher than the other two plots corresponding to Toluene and Tetrahydrofuran, which indicates least volume change of EVA in Octane. The contour plots and spatial variation of polymer volume fraction ϕ of the second EVA layer (EVA2) in the three different solvents Toluene, Tetrahydrofuran, and Octane after different time periods are shown in Figs. 14 and 15, respectively. It can be observed that the volume change and spatial variation of polymer volume fraction of EVA2 are similar to that of EVA1 in PV modules due to the fact that the thickness of silicon cell layer is very small. The time history evolution curves of EVA swelling degree of the two EVA layers in the three solvents Toluene, Tetrahydrofuran, and Octane are shown in Fig. 16. As expected, the volume of EVA layers in the PV modules increases with the penetration of solvents over time, but due to the different solubility parameters and molar volumes of three solvents, the corresponding time evolution curves of swelling degree show clear distinctions from each other.

The maximum principal stress plots of silicon solar cell layer of the PV modules in the three different solvents Toluene, Tetrahydrofuran, and Octane after 5 h, 10 h, and 15 h are shown in Fig. 17. Due to the enhanced solvent flux at the corners of EVA layers in the PV module, the stresses of silicon cell layer are higher at these marginal areas. After 5 h, the upper limit of maximum principal stress of silicon cell layer in Toluene is the highest among the three cases, with the value of 35.0 MPa, which can be ascribed to the highest swelling degree of EVA layers in this case. The maximum principal stress of silicon cell layer has the lowest value in Octane because of the lowest swelling degree of EVA layers in it. Note that the values of maximum principal stress of silicon solar cell layers in the three different solvents Toluene, Tetrahydrofuran, and Octane all increase over time as the solvents gradually penetrate into the middle area of EVA layers. After 15 h, the maximum principal stress at the outer areas of

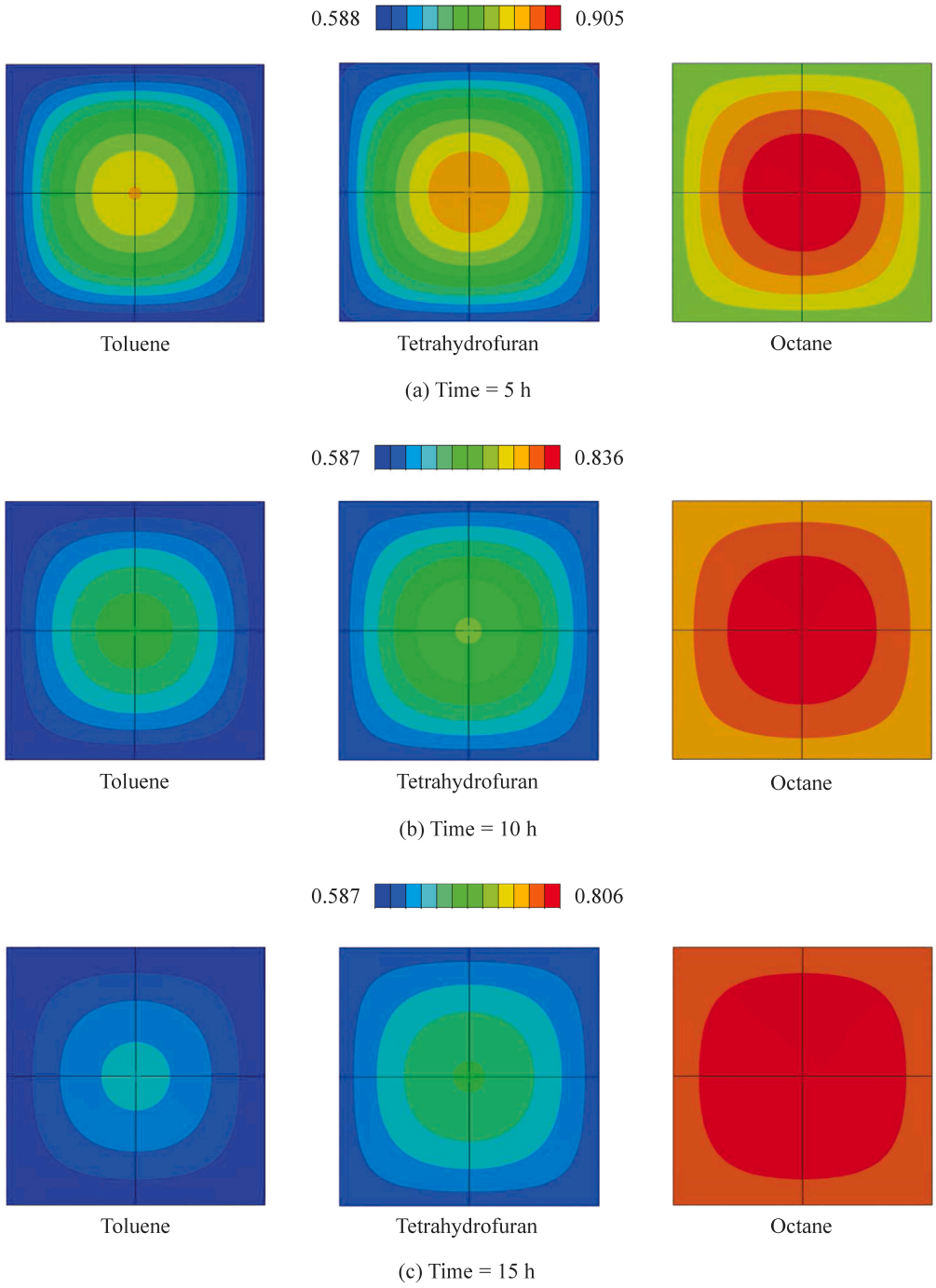

Fig. 12. The contour plots of the polymer volume fraction ϕ of the first EVA layer (EVA1) in the three different solvents Toluene, Tetrahydrofuran, and Octane after (a) 5 h, (b) 10 h, and (c) 15 h.

silicon cell layers with the three solvents reach the maximum values, indicating higher risks of silicon cracking at these areas. According to Sander, Dietrich, Pander, Ebert, and Bagdahn (2013), the fracture stress of silicon mono-crystalline was approximately 30 MPa, which might be regarded as damage criterion here. Specifically, the silicon cells are considered to be damaged when the corresponding maximum principal stress values reach this criterion. The damage plots of silicon cell layer of the PV modulus in three different solvents after 5 h, 10 h, and 15 h are shown in Fig. 18. It is noteworthy that the onset of damage affects the stress distribution in the silicon (and hence the mechanical equilibrium condition) but this is here not taken into account and is left for

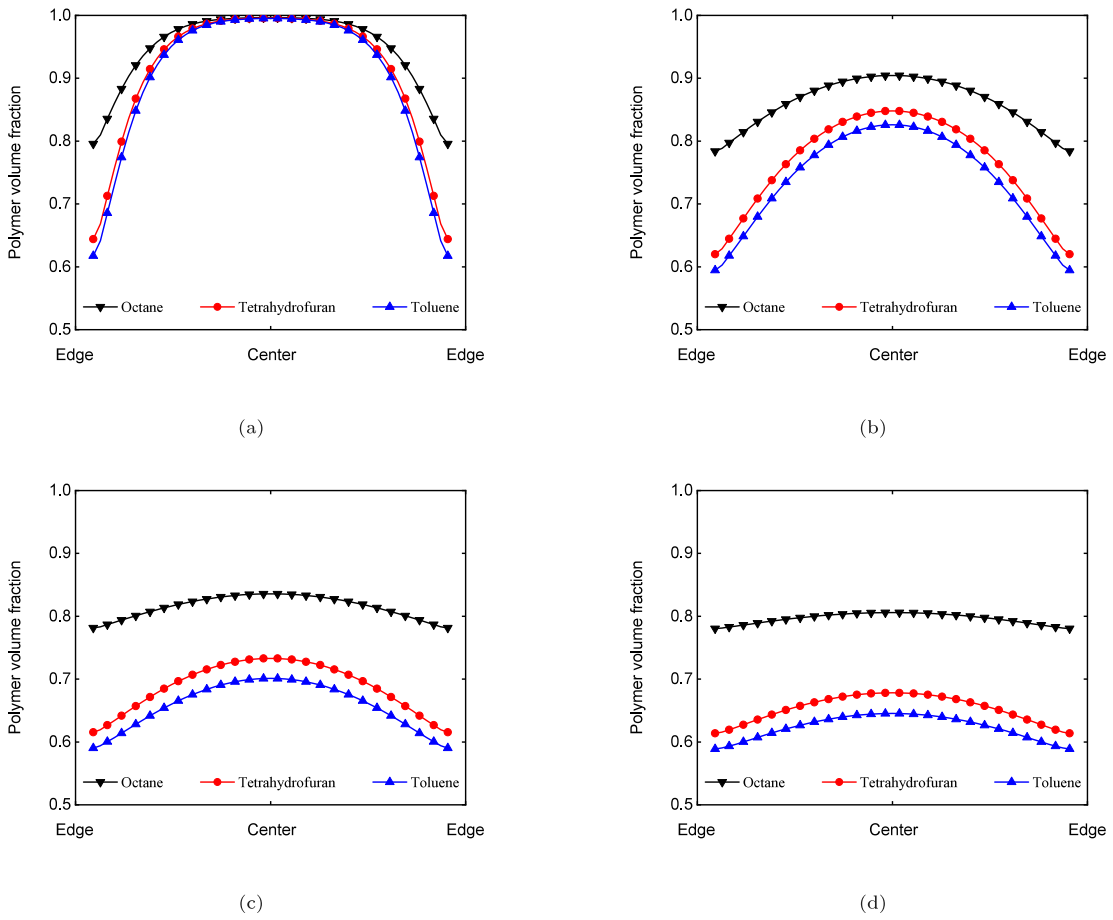

Fig. 13. The spatial variation of the polymer volume fraction ϕ of the first EVA layer (EVA1) in the three different solvents Toluene, Tetrahydrofuran, and Octane after (a) 1 h, (b) 5 h, (c) 10 h, and (d) 15 h.

future investigations. Therefore, the obtained damage distributions should be considered just as a first step towards a more detailed fracture mechanics approach. However, in the limits of such approximation, they are certainly associated with different risks of damage in the different cases.

8. Conclusions

In this work, a thermodynamically consistent large-deformation theory for the modeling of the coupled EVA polymer–solvent system has been presented in order to address the technical problems regarding the recycling of end-of-life PV modules. The computational framework accounts for the solvent diffusion in the EVA layers, swelling and elastic deformation of EVA in solvents with different solubility parameters and molar volumes, as well as effects of crosslinking and mechanical constraints. The solvent diffusion and resulting swelling of EVA layers lead to the high risks of destroying the intactness of silicon cell layers, which is the key problem in PV recycling as pointed out in Doi et al. (2001). The computational modeling in this work is a first attempt to address this technical issue that is of great importance to the PV industry.

The numerical method was firstly applied to simulate the swelling experiments of EVA in three solvents of different nature according to Mencer and Gomzi (1994), and very good agreement with the testing data has been achieved, which demonstrates the reliability of this method. Given the crosslinking of EVA in PV lamination, the second example has addressed its effects on the complex behavior of polymer–solvent system, and also taken into account the coupled shrinking effects in the presence of mechanical constraints. The reduced volume change of EVA layer with higher initial crosslinking and mechanical constraints from substrate can be predicted for the different polymer–solvent systems. The last example concerns the modeling of complete PV laminates in the 3D setting to study the deformation of silicon cell layer induced by the solvent penetration and subsequent swelling of EVA layers.

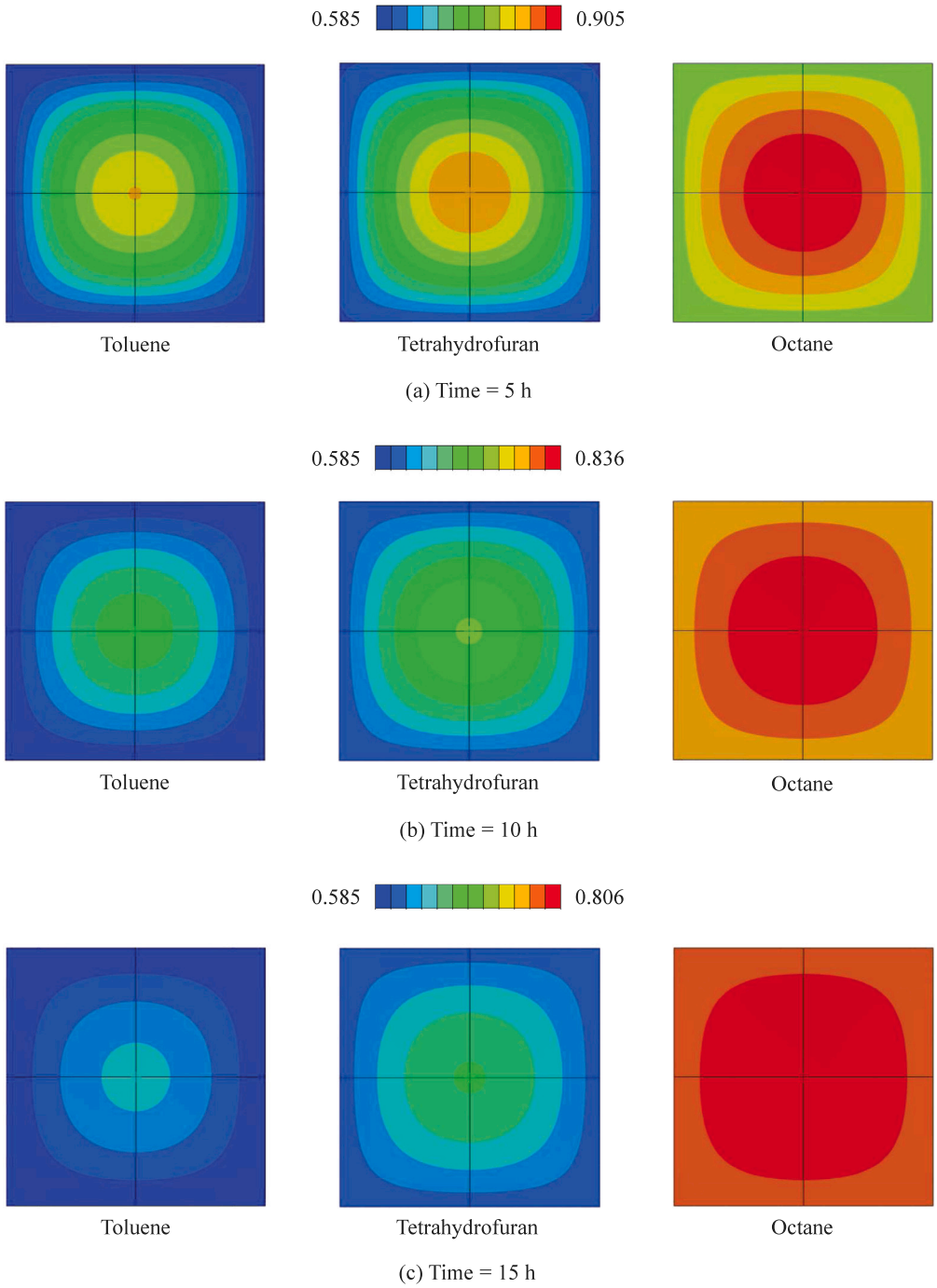

Fig. 14. The contour plots of the polymer volume fraction ϕ of the second EVA layer (EVA2) in the three different solvents Toluene, Tetrahydrofuran, and Octane after (a) 5 h, (b) 10 h, and (c) 15 h.

Solvents with different basic properties such as viscosity and molar volumes have direct impact on the coupled responses of PV modules, which further influences the recovery of nondestructive silicon wafers.

The proposed study allows to design virtual experimental procedures for the evaluation of effective impact of the coupled mechanisms on the recovery of structure-intact silicon wafers in PV recycling using the organic solvent method. Specifically, with the known basic properties of solvents and EVA copolymer used in PV modules, it is possible to identify suitable mechanical boundary conditions to guarantee the high integrity of reclaimed silicon wafers during the recycling process of end-of-life products.

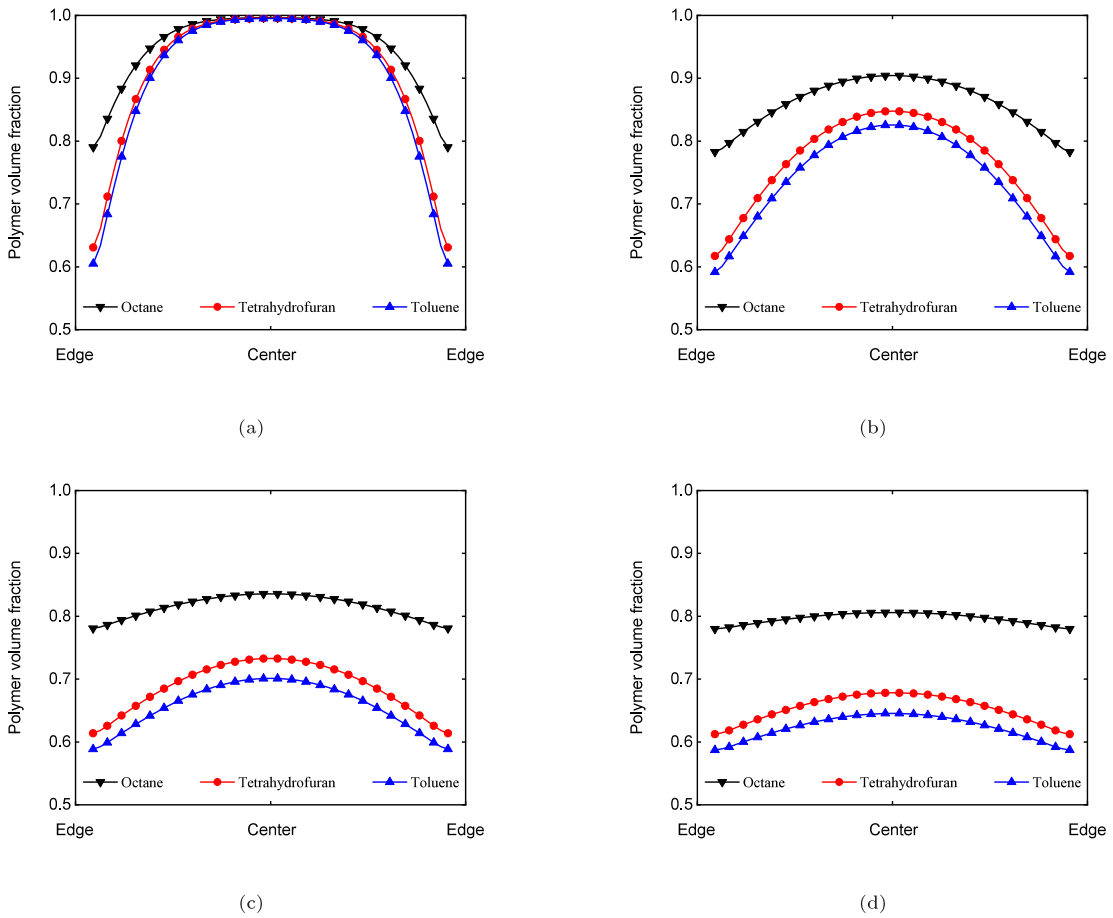

Fig. 15. The spatial variation of the polymer volume fraction ϕ of the second EVA layer (EVA2) in the three different solvents Toluene, Tetrahydrofuran, and Octane after (a) 1 h, (b) 5 h, (c) 10 h, and (d) 15 h.

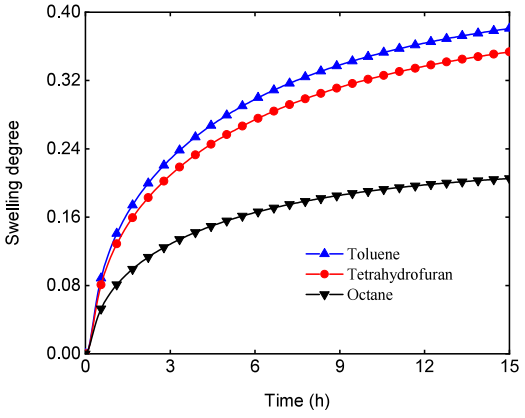

Fig. 16. The time history evolution of the EVA swelling degree in the three different solvents Toluene, Tetrahydrofuran, and Octane.

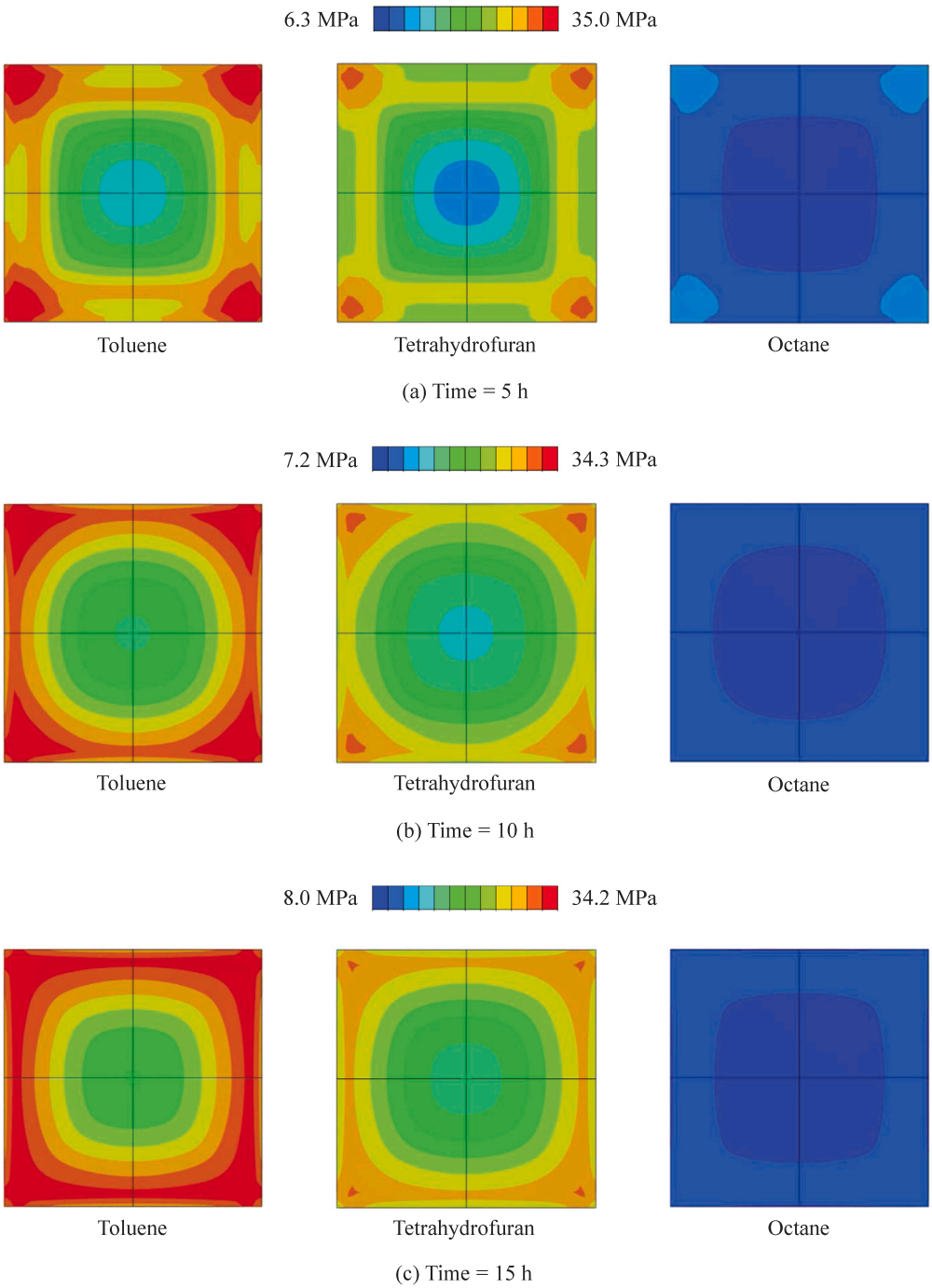

Fig. 17. The maximum principal stress plots of the silicon cell layer in the three different solvents Toluene, Tetrahydrofuran, and Octane after (a) 5 h, (b) 10 h, and (c) 15 h.

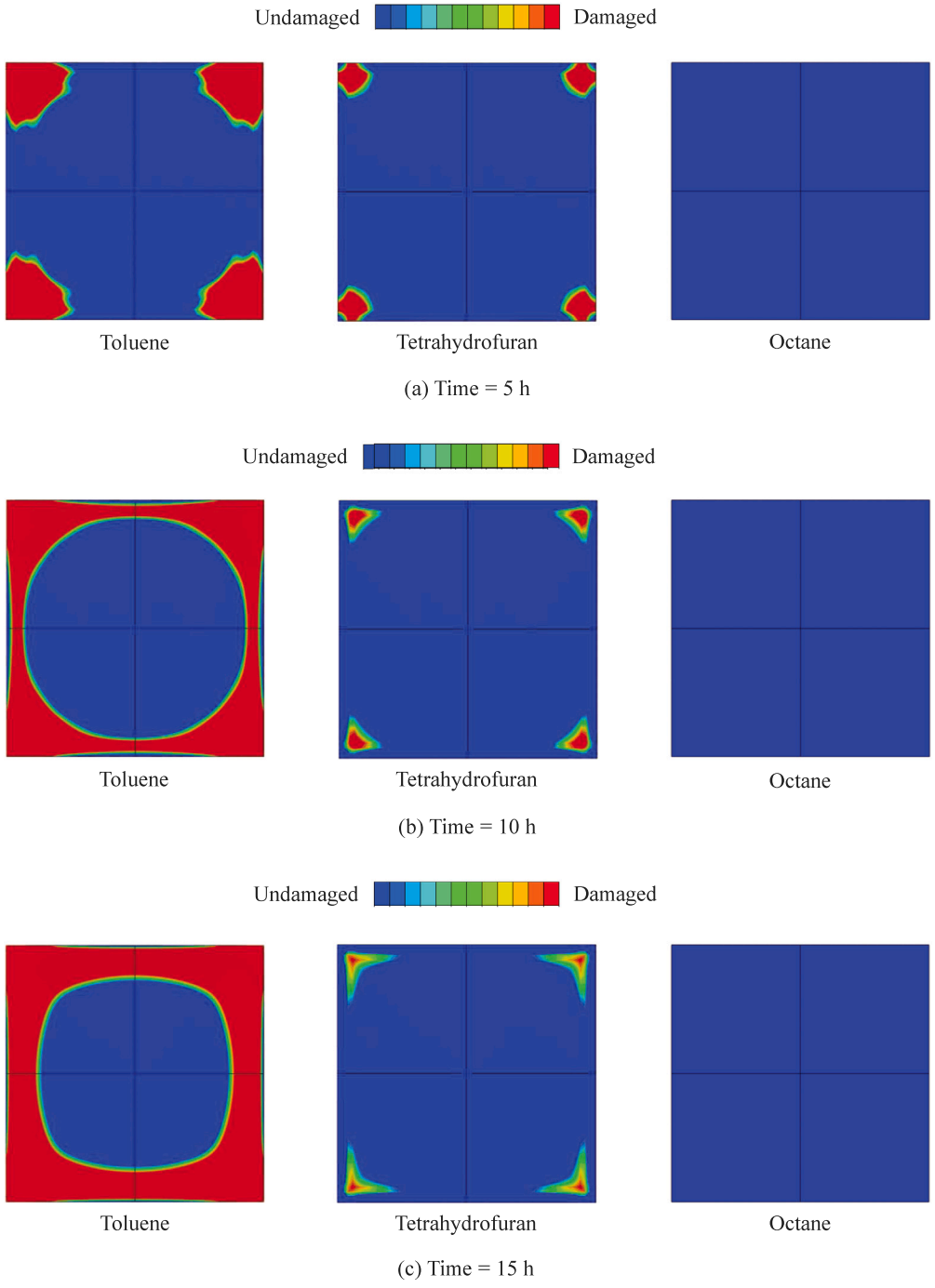

Fig. 18. The damage plots of the silicon cell layer in the three different solvents Toluene, Tetrahydrofuran, and Octane after (a) 5 h, (b) 10 h, and (c) 15 h.

Declaration of competing interest

The authors declare that they have no known competing financial interests or personal relationships that could have appeared to influence the work reported in this paper.

Data availability

Data will be made available on request.

Acknowledgments

The authors acknowledge the funding received from the European Union's Horizon 2020 research and innovation program under the Marie Skłodowska-Curie grant agreement No 861061 – Project NEWFRAC.

M. Marino gratefully acknowledges funding from the Italian Ministry of Education, University and Research MIUR (Programma per Giovani Ricercatori - anno 2017 Rita Levi Montalcini) and of Regione Lazio, Italy (POR FESR LAZIO 2014; Progetti di Gruppi di Ricerca 2020; project: BIOPMEAT, n. A0375-2020-36756).

JR is grateful to the Consejería de Economía *y* Conocimiento of the Junta de Andalucía (Spain) for financial support under the contract US-1265577-Programa Operativo FEDER Andalucía 2014–2020, and the support of the Spanish Ministerio de Ciencia, Innovación *y* Universidades, Spain the under the grant PID2019-109723GB-I00 and Consejería de Economía *y* Conocimiento of the Junta de Andalucía (Spain) under the grant P2-00595, Ministerio de Ciencia e Innovación of Spain TED2021-131649B-I00.

References

Aryan, V., Font-Brucart, M., & Maga, D. (2018). A comparative life cycle assessment of end-of-life treatment pathways for photovoltaic backsheets. *Progress in Photovoltaics: Research and Applications*, *26*(7), 443–459.

Azeumo, M. F., Germana, C., Ippolito, N. M., Franco, M., Luigi, P., & Settimio, S. (2019). Photovoltaic module recycling, a physical and a chemical recovery process. *Solar Energy Materials and Solar Cells*, *193*, 314–319.

Badiee, A., Ashcroft, I., & Wildman, R. D. (2016). The thermo-mechanical degradation of ethylene vinyl acetate used as a solar panel adhesive and encapsulant. *International Journal of Adhesion and Adhesives*, *68*, 212–218.

Baek, S., & Pence, T. J. (2009). On swelling induced degradation of fiber reinforced polymers. *International Journal of Engineering Science*, *47*(11–12), 1100–1109.

Bayat, M. R., Wang, K., & Baghani, M. (2020). Visco-hyperelastic swelling and mechanical behavior of tough pH-sensitive hydrogels: theory development and numerical implementation. *International Journal of Engineering Science*, *152*, Article 103294.

Bruton, T. (1994). Re-cycling of high value, high energy content components of silicon PV modules. In *Proc. of 12th EC-PVSEC* (pp. 303–304).

Bustamante, M. L., & Gaustad, G. (2014). Challenges in assessment of clean energy supply-chains based on byproduct minerals: A case study of tellurium use in thin film photovoltaics. *Applied Energy*, *123*, 397–414.

Chester, S. A., & Anand, L. (2011). A thermo-mechanically coupled theory for fluid permeation in elastomeric materials: application to thermally responsive gels. *Journal of the Mechanics and Physics of Solids*, *59*(10), 1978–2006.

Corcelli, F., Ripa, M., & Ulgiati, S. (2017). End-of-life treatment of crystalline silicon photovoltaic panels. An emergy-based case study. *Journal of Cleaner Production*, *161*, 1129–1142.

Corrado, M., Infuso, A., & Paggi, M. (2017). Simulated hail impacts on flexible photovoltaic laminates: testing and modelling. *Meccanica*, *52*(6), 1425–1439.

Cui, H., Heath, G., Remo, T., Ravikumar, D., Silverman, T., Deceglie, M., et al. (2022). Technoeconomic analysis of high-value, crystalline silicon photovoltaic module recycling processes. *Solar Energy Materials and Solar Cells*, *238*, Article 111592.

Czanderna, A., & Pern, F. (1996). Encapsulation of PV modules using ethylene vinyl acetate copolymer as a pottant: A critical review. *Solar Energy Materials and Solar Cells*, *43*(2), 101–181.

Deng, R., Chang, N. L., Ouyang, Z., & Chong, C. M. (2019). A techno-economic review of silicon photovoltaic module recycling. *Renewable and Sustainable Energy Reviews*, *109*, 532–550.

Deng, R., Zhuo, Y., & Shen, Y. (2022). Recent progress in silicon photovoltaic module recycling processes. *Resources, Conservation and Recycling*, *187*, Article 106612.

Dias, P., Schmidt, L., Lunardi, M. M., Chang, N. L., Spier, G., Corkish, R., et al. (2021). Comprehensive recycling of silicon photovoltaic modules incorporating organic solvent delamination–technical, environmental and economic analyses. *Resources, Conservation and Recycling*, *165*, Article 105241.

Díez, E., Camacho, J., Díaz, I., & Ovejero, G. (2014). Turbidimetric and intrinsic viscosity study of EVA copolymer–solvent systems. *Polymer Bulletin*, *71*(1), 193–206.

Doi, T., Tsuda, I., Unagida, H., Murata, A., Sakuta, K., & Kurokawa, K. (2001). Experimental study on PV module recycling with organic solvent method. *Solar Energy Materials and Solar Cells*, *67*(1–4), 397–403.

Dortdivanlioglu, B., & Linder, C. (2019). Diffusion-driven swelling-induced instabilities of hydrogels. *Journal of the Mechanics and Physics of Solids*, *125*, 38–52.

Drozdov, A. (2018). Mechanical behavior of temperature-sensitive gels under equilibrium and transient swelling. *International Journal of Engineering Science*, *128*, 79–100.

Duda, F. P., Souza, A. C., & Fried, E. (2010). A theory for species migration in a finitely strained solid with application to polymer network swelling. *Journal of the Mechanics and Physics of Solids*, *58*(4), 515–529.

Espinasse, I., Cassagnau, P., Bert, M., & Michel, A. (1994). Characterization of crosslinking of random polymer network by rheological and equilibrium swelling data. *Journal of Applied Polymer Science*, *54*(13), 2083–2089.

Farrell, C., Osman, A., Doherty, R., Saad, M., Zhang, X., Murphy, A., et al. (2020). Technical challenges and opportunities in realising a circular economy for waste photovoltaic modules. *Renewable and Sustainable Energy Reviews*, *128*, Article 109911.

Fennell, E., Leszczynski, S., Kamphus, J., & Huyghe, J. M. (2020). A strain induced softening and hardening constitutive model for superabsorbent polymers undergoing finite deformation. *International Journal of Engineering Science*, *154*, Article 103346.

Fiandra, V., Sannino, L., Andreozzi, C., Corcelli, F., & Graditi, G. (2019). Silicon photovoltaic modules at end-of-life: Removal of polymeric layers and separation of materials. *Waste Management*, *87*, 97–107.

Fiandra, V., Sannino, L., Andreozzi, C., & Graditi, G. (2019). End-of-life of silicon PV panels: A sustainable materials recovery process. *Waste Management*, *84*, 91–101.

Gagliardi, M., Lenarda, P., & Paggi, M. (2017). A reaction-diffusion formulation to simulate EVA polymer degradation in environmental and accelerated ageing conditions. *Solar Energy Materials and Solar Cells*, *164*, 93–106.

Gurtin, M. E., Fried, E., & Anand, L. (2010). *The mechanics and thermodynamics of continua*. Cambridge University Press.

Hajikhani, A., Wriggers, P., & Marino, M. (2021). Chemo-mechanical modelling of swelling and crosslinking reaction kinetics in alginate hydrogels: A novel theory and its numerical implementation. *Journal of the Mechanics and Physics of Solids*, *153*, Article 104476.

He, H., Gutierrez, Y., Young, T. M., & Schoenung, J. M. (2019). The role of data source selection in chemical hazard assessment: A case study on organic photovoltaics. *Journal of Hazardous Materials*, *365*, 227–236.

Heath, G. A., Silverman, T. J., Kempe, M., Deceglie, M., Ravikumar, D., Remo, T., et al. (2020). Research and development priorities for silicon photovoltaic module recycling to support a circular economy. *Nature Energy*, *5*(7), 502–510.
Hirschl, C., Biebl-Rydlo, M., DeBiasio, M., Mühleisen, W., Neumaier, L., Scherf, W., et al. (2013). Determining the degree of crosslinking of ethylene vinyl acetate photovoltaic module encapsulants—A comparative study. *Solar Energy Materials and Solar Cells*, *116*, 203–218.
Huang, W.-H., Shin, W. J., Wang, L., Sun, W.-C., & Tao, M. (2017). Strategy and technology to recycle wafer-silicon solar modules. *Solar Energy*, *144*, 22–31.
Kang, S., Yoo, S., Lee, J., Boo, B., & Ryu, H. (2012). Experimental investigations for recycling of silicon and glass from waste photovoltaic modules. *Renewable Energy*, *47*, 152–159.
Kim, Y., & Lee, J. (2012). Dissolution of ethylene vinyl acetate in crystalline silicon PV modules using ultrasonic irradiation and organic solvent. *Solar Energy Materials and Solar Cells*, *98*, 317–322.
Köntges, M., Kurtz, S., Packard, C., Jahn, U., Berger, K. A., Kato, K., et al. (2014). *Review of failures of photovoltaic modules*. International energy agency, IEA-PVPS, ISBN: 978-3-906042-16-9, Task 13.
Köntges, M., Oreski, G., Jahn, U., Herz, M., Hacke, P., Weiss, K.-A., et al. (2017). *Assessment of photovoltaic module failures in the field*. International energy agency, IEA-PVPS, ISBN: 978-3-906042-54-1, Task 13.
Lange, R. F., Luo, Y., Polo, R., & Zahnd, J. (2011). The lamination of (multi) crystalline and thin film based photovoltaic modules. *Progress in Photovoltaics: Research and Applications*, *19*(2), 127–133.
Lee, J.-K., Lee, J.-S., Ahn, Y.-S., Kang, G.-H., Song, H.-E., Kang, M.-G., et al. (2018). Simple pretreatment processes for successful reclamation and remanufacturing of crystalline silicon solar cells. *Progress in Photovoltaics: Research and Applications*, *26*(3), 179–187.
Lee, Y., & Tay, A. A. (2013). Stress analysis of silicon wafer-based photovoltaic modules under IEC 61215 mechanical load test. *Energy Procedia*, *33*, 265–271.
Li, K., Wang, Z., Liu, C., Wang, D., Li, G., Chen, X., et al. (2022). A green method to separate different layers in photovoltaic modules by using DMPU as a separation agent. *Solar Energy Materials and Solar Cells*, *245*, Article 111870.
Liu, Y., Kong, J., Zhuang, Y., Xing, P., Yin, H., & Luo, X. (2019). Recycling high purity silicon from solar grade silicon cutting slurry waste by carbothermic reduction in the electric arc furnace. *Journal of Cleaner Production*, *224*, 709–718.
Liu, Z., Reinoso, J., & Paggi, M. (2022a). A humidity dose-CZM formulation to simulate new end-of-life recycling methods for photovoltaic laminates. *Engineering Fracture Mechanics*, *259*, Article 108125.
Liu, Z., Reinoso, J., & Paggi, M. (2022b). Hygro-thermo-mechanical modeling of thin-walled photovoltaic laminates with polymeric interfaces. *Journal of the Mechanics and Physics of Solids*, Article 105056.
Liu, C., Zhang, Q., & Wang, H. (2020). Cost-benefit analysis of waste photovoltaic module recycling in China. *Waste Management*, *118*, 491–500.
Lovato, É. S., Donato, L. M., Lopes, P. P., Tanabe, E. H., & Bertuol, D. A. (2021). Application of supercritical CO2 for delaminating photovoltaic panels to recover valuable materials. *Journal of CO2 Utilization*, *46*, Article 101477.
Mencer, H., & Gomzi, Z. (1994). Swelling kinetics of polymer-solvent systems. *European Polymer Journal*, *30*(1), 33–36.
Mezzasalma, S. A., Abrami, M., Grassi, G., & Grassi, M. (2022). Rubber elasticity of polymer networks in explicitly non-Gaussian states. Statistical mechanics and LF-NMR inquiry in hydrogel systems. *International Journal of Engineering Science*, *176*, Article 103676.
Nain, P., & Kumar, A. (2020). Ecological and human health risk assessment of metals leached from end-of-life solar photovoltaics. *Environmental Pollution*, *267*, Article 115393.
Nevala, S.-M., Hamuyuni, J., Junnila, T., Sirviö, T., Eisert, S., Wilson, B. P., et al. (2019). Electro-hydraulic fragmentation vs conventional crushing of photovoltaic panels–Impact on recycling. *Waste Management*, *87*, 43–50.
Padhi, S., Raju Achary, P. G., & Nayak, N. C. (2015). Molecular transport behaviour of organic solvents through halloysite nanotubes filled ethylene–vinyl acetate copolymer. *Bulletin of Materials Science*, *38*(4), 925–933.
Padoan, F. C., Altimari, P., & Pagnanelli, F. (2019). Recycling of end of life photovoltaic panels: A chemical prospective on process development. *Solar Energy*, *177*, 746–761.
Paggi, M., Berardone, I., Infuso, A., & Corrado, M. (2014). Fatigue degradation and electric recovery in Silicon solar cells embedded in photovoltaic modules. *Scientific Reports*, *4*(1), 1–7.
Paggi, M., Corrado, M., & Berardone, I. (2016). A global/local approach for the prediction of the electric response of cracked solar cells in photovoltaic modules under the action of mechanical loads. *Engineering Fracture Mechanics*, *168*, 40–57.
Paggi, M., Corrado, M., & Rodriguez, M. A. (2013). A multi-physics and multi-scale numerical approach to microcracking and power-loss in photovoltaic modules. *Composite Structures*, *95*, 630–638.
Paggi, M., Kajari-Schröder, S., & Eitner, U. (2011). Thermomechanical deformations in photovoltaic laminates. *The Journal of Strain Analysis for Engineering Design*, *46*(8), 772–782.
Pang, S., Yan, Y., Wang, Z., Wang, D., Li, S., Ma, W., et al. (2021). Enhanced separation of different layers in photovoltaic panel by microwave field. *Solar Energy Materials and Solar Cells*, *230*, Article 111213.
Park, J., Kim, W., Cho, N., Lee, H., & Park, N. (2016). An eco-friendly method for reclaimed silicon wafers from a photovoltaic module: from separation to cell fabrication. *Green Chemistry*, *18*(6), 1706–1714.
Prasad, D., Sanjana, B., Kiran, D. S., Kumar, P. S., & Ratheesh, R. (2022). Process optimization studies of essential parameters in the organic solvent method for the recycling of waste crystalline silicon photovoltaic modules. *Solar Energy Materials and Solar Cells*, *245*, Article 111850.
Sah, D., Kumar, S., et al. (2022). Recovery and analysis of valuable materials from a discarded crystalline silicon solar module. *Solar Energy Materials and Solar Cells*, *246*, Article 111908.
Sander, M., Dietrich, S., Pander, M., Ebert, M., & Bagdahn, J. (2013). Systematic investigation of cracks in encapsulated solar cells after mechanical loading. *Solar Energy Materials and Solar Cells*, *111*, 82–89.
Sauerwein, M., & Steeb, H. (2020). Modeling of dynamic hydrogel swelling within the pore space of a porous medium. *International Journal of Engineering Science*, *155*, Article 103353.
Schulze, S.-H., Apel, A., Daßler, D., & Ehrich, C. (2015). Cure state assessment of EVA-copolymers for PV-applications comparing dynamic-mechanical, dielectric and calorimetric properties. *Solar Energy Materials and Solar Cells*, *143*, 411–417.
Shin, J., Park, J., & Park, N. (2017). A method to recycle silicon wafer from end-of-life photovoltaic module and solar panels by using recycled silicon wafers. *Solar Energy Materials and Solar Cells*, *162*, 1–6.
Tammaro, M., Rimauro, J., Fiandra, V., & Salluzzo, A. (2015). Thermal treatment of waste photovoltaic module for recovery and recycling: Experimental assessment of the presence of metals in the gas emissions and in the ashes. *Renewable Energy*, *81*, 103–112.
Tammaro, M., Salluzzo, A., Rimauro, J., Schiavo, S., & Manzo, S. (2016). Experimental investigation to evaluate the potential environmental hazards of photovoltaic panels. *Journal of Hazardous Materials*, *306*, 395–405.
Tanaka, T., & Fillmore, D. J. (1979). Kinetics of swelling of gels. *The Journal of Chemical Physics*, *70*(3), 1214–1218.
Tao, J., & Yu, S. (2015). Review on feasible recycling pathways and technologies of solar photovoltaic modules. *Solar Energy Materials and Solar Cells*, *141*, 108–124.
Wallner, G. M., Adothu, B., Pugstaller, R., Costa, F. R., & Mallick, S. (2022). Comparison of crosslinking Kinetics of UV-Transparent ethylene-vinyl acetate copolymer and polyolefin elastomer encapsulants. *Polymers*, *14*(7), 1441.
Wang, X., Tian, X., Chen, X., Ren, L., & Geng, C. (2022). A review of end-of-life crystalline silicon solar photovoltaic panel recycling technology. *Solar Energy Materials and Solar Cells*, *248*, Article 111976.

Weckend, S., Wade, A., & Heath, G. A. (2016). *End of life management: solar photovoltaic panels*: *Tech. rep*, National Renewable Energy Lab.(NREL), Golden, CO (United States).

Wriggers, P. (2008). *Nonlinear finite element methods*. Springer Science & Business Media.

Xu, X., Lai, D., Wang, G., & Wang, Y. (2021). Nondestructive silicon wafer recovery by a novel method of solvothermal swelling coupled with thermal decomposition. *Chemical Engineering Journal*, *418*, Article 129457.

Zäh, D., & Miehe, C. (2015). Multiplicative electro-elasticity of electroactive polymers accounting for micromechanically-based network models. *Computer Methods in Applied Mechanics and Engineering*, *286*, 394–421.

Zhang, L., & Xu, Z. (2016). Separating and recycling plastic, glass, and gallium from waste solar cell modules by nitrogen pyrolysis and vacuum decomposition. *Environmental Science and Technology*, *50*(17), 9242–9250.